Meso- to micro-scale modeling of atmospheric stability effects on wind turbine wake behavior in complex terrain

Adam S Wise[1], James M T Neher[1], Robert S Arthur[2], Jeffrey D Mirocha[2], Julie K Lundquist[3,4], and Fotini K Chow[1]

[1]Department of Civil and Environmental Engineering, University of California, Berkeley, Berkeley, California, USA
[2]Lawrence Livermore National Laboratory, Livermore, California, USA
[3]Department of Atmospheric and Oceanic Sciences, University of Colorado Boulder, Boulder, Colorado, USA
[4]National Renewable Energy Laboratory, Golden, Colorado, USA

Correspondence: Adam S Wise (adamwise@berkeley.edu)

Abstract. ~~Most detailed modeling and simulation studies of wind turbine wakes have considered flat terrain scenarios. Wind turbines, however, are commonly sited in mountainous or hilly terrain to take advantage of accelerating flow over ridgelines. In addition to topographic acceleration, other turbulent flow phenomena commonly occur in complex terrain, and often depend upon the thermal stratification of the atmospheric boundary layer. Enhanced understanding of~~ Terrain-induced flow phenomena modulate wind turbine performance and wake behavior in ways that are not adequately accounted for in typical wind turbine wake ~~interaction with these terrain-induced flow phenomena can significantly improve wind farm siting, optimization, and control~~and wind plant design models. In this ~~study~~work, we simulate ~~conditions observed during the Perdigão field campaign in 2017, consisting of~~ flow over two parallel ridges with a wind turbine ~~located on top of~~ on one of the ridges, focusing on conditions observed during the Perdigão field campaign in 2017. Two case studies are selected to be representative of typical flow conditions at the site, including the effects of atmospheric stability: a stable case where a mountain wave occurs (as in ~50% of the nights observed), and a convective case where a recirculation zone forms in the lee of the ridge with the turbine (as occurred over 50% of the time with upstream winds normal to the ridgeline). We use the Weather Research and Forecasting model (WRF)~~nested down~~, dynamically downscaled from the mesoscale (6.75 km resolution) to micro-scale large-eddy simulation (LES) at 10 m resolution, ~~with~~ where a generalized actuator disk (GAD) wind turbine parameterization is used to simulate turbine wakes. ~~Two case studies are selected, a stable case where a mountain wave occurs and a convective case where a recirculation zone forms in the lee of the ridge with the turbine. The~~ We compare the WRF-LES-GAD model ~~is validated against~~ results to data from meteorological towers, ~~soundings~~lidars, and a tethered lifting system, showing good qualitative and quantitative agreement for both ~~cases. Comparisons with scanning Doppler lidar data for the stable case show that the overall characteristics of the mountain wave are well-captured, although the wind speed is underestimated. For the convective case, the size of the recirculation zone within the valley shows good agreement. The~~ case studies. Significantly, the wind turbine wake ~~behavior shows dependence on atmospheric stability, with~~ shows different amounts of vertical deflection from the terrain and persistence downstream ~~for the stable and convective conditions. For~~ in the two stability regimes. In the stable case, the wake follows the terrain along with the mountain wave and deflects downwards by nearly 100 m below hub-height at four rotor diameters downstream. ~~For~~ In the convective case, the wake deflects above the recirculation zone over ~~50~~40 m above

hub-height at the same downstream distance. ~~This study demonstrates the ability of the~~ Overall, the WRF-LES-GAD model is able to capture the ~~expected behavior of~~ observed behavior of the wind turbine wakes~~in regions of complex terrain , and thereby to potentially~~, demonstrating the model's ability to represent wakes over complex terrain for two distinct and representative atmospheric stability classes, and, potentially, to improve wind turbine siting and operation in hilly landscapes.

1 Introduction

Wind turbines are commonly sited in ~~mountainous and hilly~~ complex terrain to take advantage of topographic flow enhancement, such as the acceleration of flow over ridge lines and hill tops. ~~The complexity of the interaction between wind turbine wakes and complex terrain has historically limited research studies to wind tunnel experiments and numerical simulations with simple Gaussian and sinusoidal hills (see Porté-Agel et al. (2020) for a recent review on wind farm flows and topography).~~ In addition to topographic acceleration, other terrain-induced flow phenomena in the atmospheric boundary layer (ABL) ~~may~~ affect wind turbine performance and wake propagation and characteristics (Xia et al., 2021; Draxl et al., 2021). These microscale processes include mountain/lee waves (and associated rotors), hydraulic jumps, valley flows, ~~flow separation and~~ and flow separation/recirculation (Fernando et al., 2019; Baines, 1998).

The dynamics of terrain-induced flow phenomena can vary widely based on the time of the day, with lee waves only occurring during stably stratified conditions, typical at night, and flow separation or recirculation often occurring during daytime convective ~~conditions.~~ (or unstably stratified) conditions. Interactions of the terrain with different stability conditions thus impacts both the background flow and the resulting turbine performance. The difficulty of capturing the interaction between wind turbine wakes and complex terrain has historically limited research studies to wind tunnel experiments and numerical simulations with simple Gaussian and sinusoidal hills (see Porté-Agel et al. (2020) for a recent review on wind farm flows and topography). Additionally, turbine wake models used for designing wind farms typically do not account for terrain-induced flow phenomena and their effects on turbine wake behavior. Increased knowledge of wind flows in complex terrain is therefore critical to improve predictions to support growing wind energy resources (Veers et al., 2019).

~~Many studies have demonstrated how wind turbine wake behavior is strongly affected by ABL stability conditions (Iungo et al., 2013; Mi . The wake, as a result of wind turbine operation, induces a decrease in wind speed and increase in turbulence, resulting in lower than expected power output and increased structural loading in downstream turbines (Lissaman, 1979; Taylor, 1990; Thomsen and Sørensen . During unstable or convective conditions (typically during the daytime for onshore locations), wakes diffuse rapidly and meander due to large-scale eddies that are present. During stable conditions, wake deficits can persist for much greater downstream distances (Hirth and Schroeder, 2013).~~

~~Large-eddy~~

In the present work, we use large-eddy simulation (LES) ~~is a common and useful tool for simulating the ABL~~to examine the wake behavior of a wind turbine situated in complex terrain. LES explicitly solves for the most energetic eddies while parameterizing the effects of the smaller turbulent length scales on the resolved-scale flow. ~~This allows for resolving transient turbulent~~ LES can therefore capture transient turbulent flow structures, which are important features of ~~boundary layer turbulence and~~

wind the ABL that interact with turbine wakes. LES is While LES is computationally expensive, and thus requires the use of substantial high-performance computing resources, LES is increasingly complementing and even in many in some cases replacing lower-fidelity techniques as a means to investigate wind turbine wake effects (see Stevens and Meneveau (2017) for a recent review). One example is Shamsoddin and Porté-Agel (2017), who modeled a wind farm sited on a single hill and validated their model using data from Tian et al. (2013) for a neutral ABL.

In the present work, Specifically, we utilize the LES capability of the Weather Research and Forecasting (WRF) model (Skamarock et al., 2008; Powers et al., 2017) together with an actuator disk wind turbine model to simulate wind turbine wake behavior in complex hilly terrain. In addition to running standalone, idealized WRF-LES simulations, we take advantage of the more complex for our simulations. The multi-scale modeling framework available within WRF. This multi-scale framework in WRF dynamically downscales mesoscale forcing to microscale LES using a grid nesting approach, with lateral boundary conditions provided from each nest's parent domain. Such setups can provide LES with more realistic time-varying inflow conditions directly from the mesoscale simulations, as these setups include the large scale forcing that results from dynamic downscaling capturing a wider range of atmospheric phenomena and more realistic turbulence compared to conventional idealized LES setups (Wiersema et al., 2020).

Moreover, implementation Implementation of a wind turbine actuator disk parameterization within the nested LES domain provides a unique high-fidelity simulation framework for wind turbine wake prediction in turbulent flow settings under more realistic environmental and atmospheric forcing conditions. This study utilizes a generalized actuator disk (GAD) wind turbine parameterization on the finest domain following Mirocha et al. (2014). In the GAD parameterization, thrust and rotational forces computed at the turbine's blades are averaged over a discretized two-dimensional disk formed by their rotation. These forces are then applied to the flow surrounding the turbine, capturing both the velocity deficit and rotation of the wake, which simpler parameterizations (such as the Fitch et al. (2013) wind farm parameterization) neglect. The GAD tool , hereinafter referred to as WRF-LES-GAD for the model in its entirety, has been previously validated and shown to capture turbine-airflow interactions and wake behavior well at grid resolutions of 10 m in simple terrain (Mirocha et al., 2015; Aitken et al., 2014; Marjanovic et al., 2017; Arthur et al., 2020). However, the multiscale WRF-LES-GAD framework (hereinafter used to denote the model in its entirety) has yet to be evaluated in complex terrain where the combination of terrain and thermal stratification directly affects the flow and impacts operating turbines.

The test location chosen in this study is that of the Perdigão field campaign (Fernando et al., 2019), which took place in 2017 in Portugal. The Perdigão experiment characterized the flow over two parallel ridges with a wind turbine located on the southwest ridge and provided valuable data for characterizing wind turbine wakes in complex terrain (Menke et al., 2018; Barthelmie and Pryor, 2019; Wildmann et al., 2018, 2019). Menke et al. (2018) classified wind turbine wake behavior based on atmospheric stability using scanning Doppler lidars at Perdigão. They identified , identifying four different cases for based on the stratification: a "stable + mountain wave" case where the wake advected deflected downwards following the terrain, "stable" and "neutral" cases where the wake remained at a constant height above sea level, and "unstable" cases where the wake advected deflected upwards. Barthelmie and Pryor (2019) similarly characterized wake behavior at Perdigão based on atmospheric stability. Using measurements averaged over longer time periods (10 minutes compared to 24 seconds

in Menke et al. (2018)), they ~~infer~~ inferred that all wakes were initially lofted and then strongly influenced by stability, with wake centers moving downwards in unstable conditions and also generally moving downwards but remaining at greater heights during stable conditions. The different findings in these two studies motivate the need to further study wind turbine wakes in complex terrain~~and to accompany the field data analysis with numerical models~~.

Two fine-scale ($\Delta x = 10$ m) LES modeling studies of the Perdigão campaign have been ~~presented in the literature thus far~~conducted with a wind turbine parameterization, both in idealized conditions with neutral stability. Berg et al. (2017) performed idealized LES of the Perdigão site in neutral atmospheric stability conditions and showed that the steep terrain in Perdigão resulted in the formation of a recirculation zone with which the wake did not interact. Instead, the wake advected at a constant height above sea level like the "neutral" case characterized by Menke et al. (2018). Dar et al. (2019) also ~~modeled~~ simulated the Perdigão site using idealized LES to examine the self-similarity of wind turbine wake behavior as a function of varying terrain complexity under neutral stratification. They found that self-similarity is preserved for a shorter distance compared to what is observed in flat terrain and that the wake propagation was similar to that seen by Berg et al. (2017). ~~Both of these studies considered idealized conditions with neutral atmospheric stability.~~ There have also been been two relatively coarse nested LES studies of the Perdigão campaign by Connolly et al. (2021) and Wagner et al. (2019), where grid resolutions of 150 m and 200 m were used, respectively, with both utilizing the LES capability of WRF. The findings from these studies have provided guidance for the setup used in this study (as discussed in Section 3) but their setups are too coarse to resolve a utility-scale wind turbine with a rotor diameter of 80 m.

The ~~focus~~ goal of this work is to ~~model realistic atmospheric conditions and the associated turbulent flow phenomena to better understand wind turbine wake propagation in complex terrain, using~~ examine the ability of the WRF-LES-GAD framework to capture terrain-induced flows and their interaction with an operating wind turbine at the Perdigão site ~~as the test location (described~~ (described further in Sect. 2)~~. Specifically, we analyze how the vertical deflection and dissipation of the wake varies based on atmospheric stability. In our modeling approach, we use the WRF-LES-GAD framework, first in an idealized setting and then in a multi-scale nested domain setup with real atmospheric forcing (Sect. 3). The~~ , to thereby demonstrate the efficacy of mesoscale-to-microscale coupled simulations to improve wind plant simulations in complex terrain. We focus on two distinct but representative case studies with different atmospheric stability regimes, convective and stable, both of which were commonly observed during the field experiment. We validate the predicted flow structure ~~during stable and convective case studies is analyzed and validated by comparing with scanning lidars,~~ and turbine wake behavior during each case study using comparisons with observations from meteorological towers, ~~soundings~~scanning lidars, and a tethered lifting system (Sect. 4). ~~These findings are followed by~~ Furthermore, we present a detailed analysis of the ~~wind turbine wake behavior in the given cases~~turbine wake in both stability regimes in order to comment on the discrepancy in the observational studies discussed above.

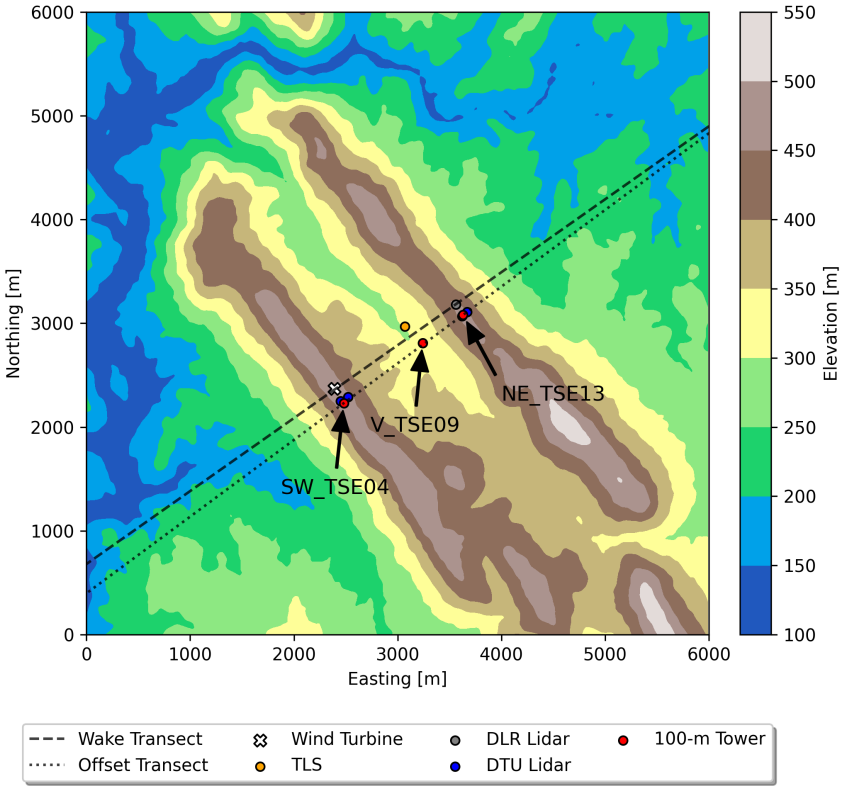

Figure 1. Terrain and layout of the Perdigão site showing the location of relevant instrumentation. The Wake and Offset Transects are used for analysis later in this paper. Each of the three 100 m meteorological towers is labeled following the naming convention in the publicly available dataset corresponding to their geographic location.

2 Case Study

2.1 Overview of the Perdigão campaign

The Perdigão field campaign was a European Union - United States collaboration of over 70 scientists, engineers, and support personnel. The Perdigão site, named for a village located near the Vale do Cobrão in eastern Portugal, consists of two parallel ridges with a 2 megawatt (MW) wind turbine located on the southwest ridge (see Fig. 1). This site was selected because the straight valley extends over 2 km in distance, suggesting that the flow could be representative of an idealized two-dimensional valley flow in nature. Additionally, the annual climatology showed that common wind directions measured at ridge-top are perpendicular to the ridges (Fernando et al., 2019).

During the intensive operation period (IOP) from 1 May 2017 to 15 June 2017, a comprehensive, high-resolution dataset was collected. Instrumentation included 100-m meteorological towers (hereinafter referred to as met towers), ~~radiosondes,~~ lidars, a tethered lifting system (TLS)~~and additional instrumentation including~~ , and numerous shorter meteorological towers and radiometers. The instrumentation of interest is discussed here, and the layout of the Perdigão field site is shown in Fig. 1.

Three 100-m met towers were placed along a transect roughly perpendicular to the ~~ridge~~ ridges (see Fig. 1). ~~One tower was located on the southwest ridge (~~SW_TSE04~~), another in the valley (V_TSE09), and the third on the northeast ridge (NE_TSE13). SW_TSE04~~, located approximately 150 m southeast of the wind turbine laterally along the ridgeline, is representative of inflow conditions. ~~The three 100-m met~~ V_TSE09 is located in the valley, and NE_TSE13 is on the northeast ridge. These three towers have booms angled at 135° from north located at heights of 10, 20, 40, 60, 80, and 100 m with sonic anemometers sampling three-dimensional ~~wind~~ velocity at 20 Hz. In this paper, data representative of near surface winds (10 m) and at hub-height (80 m) are examined. ~~In addition to sonic anemometers, temperature sensors are available at multiple heights. The temperature sensors at~~ Temperature sensors available at 10 m and 100 m are used to characterize atmospheric stability using a simple temperature gradient similar to Menke et al. (2019).

~~A radiosonde launching site was located in the valley (Fig. 1) and provides vertical profiles of pressure, temperature, wind speed, and wind direction. The sondes were launched every 6 hours at approximately 00:00, 06:00, 12:00, 18:00 UTC for the duration of the campaign. During periods of interest, additional soundings were launched.~~

A tethered lifting system (TLS) from the University of Colorado, Boulder, was also launched from the valley. The TLS is a unique device that is able to obtain in-situ measurements of wind speed, wind direction, and temperature aloft at 1 kHz (Balsley, 2008). ~~Additionally,~~ GPS measurements of latitude, longitude, and altitude ~~were~~ are sampled at 5 s. When in profiling mode, the TLS ascends and descends at ~~a rate of approximately~~ ~0.3 m s^{-1} and covers a vertical range of ~~close to~~ ~400 m. The capabilities of the TLS have been demonstrated in several field campaigns, including a previous wind turbine wake investigation (Lundquist and Bariteau, 2015).

Simulation results are also compared with scanning Doppler lidar data. The first is a scanning lidar operated by the German Aerospace Center (DLR) located on the northeast ridge (Wildmann et al., 2018). This lidar's scanning trajectory is perpendicular to the wind turbine rotor allowing for the wake to be captured in addition to relevant flow features in the valley. The second set of scanning lidars used here were operated by the Danish Technical University (DTU) (Menke et al., 2020). Four lidars, two on each ridge, scanned a transect perpendicular to the valley. Because of how the lidars are arranged, a multi-Doppler lidar scan of the valley, the two ridges, and the surrounding area can be formed. This multi-Doppler lidar scan does not capture the wind turbine wake but does show microscale features that interact with the wind turbine wake (as seen later in Figure 4).

2.2 Case Studies and Phenomena of Interest

Two terrain-induced flow features characteristic of the field site are of interest for the present work: (a) mountain waves and (b) recirculation zones. ~~These flow features may occur~~ , which occur frequently at the Perdigão site depending on the time of day (Menke et al., 2019; Fernando et al., 2019; Wagner et al., 2019)~~and are characteristic of the site, in general~~. Fernando et al. (2019) found that mountain waves occurred for almost 50% of the nights during the IOP while Menke et al. (2019) found that

recirculation occurred over 50% of the time when the wind direction was perpendicular to the ridges. To help select appropriate time periods representing mountain waves and recirculation zones, we examine a few stability parameters.

Mountain waves can occur when stably stratified flow approaches a topographic disturbance, such as a mountain ridge. These waves can be ~~characterized by the Froude number:~~ described using a ratio of inertial to buoyant forces represented by the internal Froude number (Stull, 1988),

$$Fr = \frac{U}{hN}\frac{\pi U}{WN}, \tag{1}$$

where ~~h~~ W is the mountain ridge ~~height~~width (defined for the southwest ridge of Perdigão to be 586.5 m on average according to Palma et al. (2020)), U is the free stream wind speed, and N is the Brunt-Väisälä frequency, defined as:

$$N = \sqrt{\frac{g}{\theta}\frac{d\theta}{dz}}. \tag{2}$$

Here g is the gravitational constant, θ is the potential temperature of the environment, and $\frac{d\theta}{dz}$ is the lapse rate or vertical gradient in potential temperature. ~~For small Froude numbers (<1)~~ The internal Froude number can also be defined as the ratio of the natural wavelength of the air ($\lambda = 2\pi U N^{-1}$) to the effective wavelength of the mountain ridge ($2W$).

For subcritical flow ($Fr < 1$), when wind speeds are low or the stability is very strong, ~~the wavelength of the mountain wave is short~~ λ is much shorter than $2W$ resulting in weak mountain waves. Mountain waves resonate when ~~the Froude number is approximately equal to 1~~ $Fr \sim 1$, resulting in strong up and downdrafts where rotors (and potentially hydraulic jumps) are present (Jackson et al., 2013). When wind speeds are strong and stability is weak, ~~the Froude number is large (>1)~~ $Fr > 1$ and flow is supercritical resulting in long wavelengths with the potential for reverse flow in the lee of the mountain.

Neutral and convective conditions represent ~~a theoretically infinite Froude number. For Fr$\approx \infty$, waves do not occur; instead,~~ the theoretical case of Fr $\sim \infty$, when a turbulent mountain wake with recirculation forms instead of mountain waves. Relevant to this study are Fr~~≈ 1~~ ≈ 1 during stable conditions and Fr~~$\approx \infty$~~ $\approx \infty$ during convective conditions. For more information regarding mountain waves, the reader is referred to ~~(Baines, 1998; Jackson et al., 2013)~~Stull (1988), Baines (1998) and Jackson et al. (2013).

Quantifying atmospheric stability in complex terrain is an active research area. Using a gradient Richardson number is difficult because of the effect of terrain-induced flow-speedup over the ridge affecting the shear terms~~as mentioned by Menke et al. (2019) . Additionally,~~ (Menke et al., 2019). Bodini et al. (2020) calculated the Obukhov length ~~at the~~ for Perdigão and found that it was not very powerful in predicting dissipation rate. Despite ~~its limited ability to quantify atmospheric stability in complex terrain~~this, the Obukhov length is still useful for selecting stable and unstable case studies. The Obukhov length, L, is defined as ~~follows:~~

$$L = \frac{-u_*^3\theta}{\kappa g \overline{w'\theta'}}, \tag{3}$$

where ~~$u*$~~ u_* is the friction velocity, κ is the von Kármán constant (taken as 0.4), ~~g is the earth's gravitational acceleration~~w is the vertical velocity, and $w'\theta'$ is the surface heat flux. The prime denotes fluctuations and the overbar a mean. The friction

velocity is defined as ~~:~~

$$u_* = \left(\overline{u'w'}^2 + \overline{v'w'}^2\right)^{1/4} \quad (4)$$

The Obukhov length and friction velocity~~are calculated for~~ , valid for the surface layer, are calculated at SW_TSE04 using 5 minute statistics ~~and at a height of 10 m, which is where~~ from the lowest sensors ~~are available~~ available at 10 m. Obukhov lengths between 0 and 500 are considered stable and 0 to -500 unstable.

~~Because the focus of the present work is not on the strength of the stability, but whether the period of interest is more broadly stably or unstably stratified, in~~ In addition to the Obukhov length~~we use~~ , the potential temperature gradient between 10 m and 100 m ~~on the met tower of the southwest ridge~~ at SW_TSE04 is used as a proxy for atmospheric stability throughout this study and when comparing observations with the model. Note that SW_TSE04 was not outfitted with any pressure sensors; therefore, the potential temperature is approximated by $\theta \approx T + (g/C_p) \cdot z$ where $(g/C_p) = 0.0098$ K m^{-1} as was done by Menke et al. (2019). ~~A positive temperature gradientindicates stably stratified flow and a negative temperature gradient indicates unstable or convectively driven flow.~~ Fig. 2 shows wind speed, direction, temperature gradient, and Obukhov length for two different dates during the field campaign, and representative time periods are selected from these for the stable and convective case studies. The met tower measured periods of counter-gradient heat fluxes during both stable and convective conditions but not during the time periods selected for this tower location.

2.2.1 Case 1: Stable Conditions

The early morning of 14 June 2017 shows typical stably-stratified conditions as indicated by a positive temperature gradient and Obukhov length in Fig. 2(e) and Fig. 2(g), respectively. From 04:00 to 06:00 UTC (05:00 to 07:00 local time, with sunrise at 06:02 local time), the hub-height wind direction is relatively constant between 200° and 220° (Fig. 2(c)). These wind directions are close to a southwesterly wind of 215°, ~~which corresponds to being~~ perpendicular to the ridges~~due to their orientation. The~~ . The average wind speed is ~~between 5 and 7.5~~ 6.3 m s^{-1}, a ~~range~~ speed in which the turbine will operate and generate wake effects. ~~Figure ?? shows that the Brunt-Väisälä frequency is close to 0.04~~Using the average wind speed (6.3 m s^{-1}~~at the beginning of the period decreasing to 0.02 s~~), temperature gradient or lapse-rate (0.031 K m^{-1}~~at the end of the period. Using the 80 mwind speed from SW_TSE04, the Froude number begins the period close to 0.7, approaches 1.0 during the middle of the period , and then decreases at the end of the period as the sun begins to rise. During this period, two soundings were launched and the TLS was operational.~~), potential temperature of the environment (296.7 K), and width of the southwestern ridge of Perdigão (586.5 m), the average internal Froude number during the period of interest is calculated to be 1.05. With a Froude number close to one, we expect a resonant mountain wave to occur.

~~Calculated Brunt-Väisälä frequency (N) and Froude number (Fr) during the stable case study. The period of interest is highlighted in red.~~

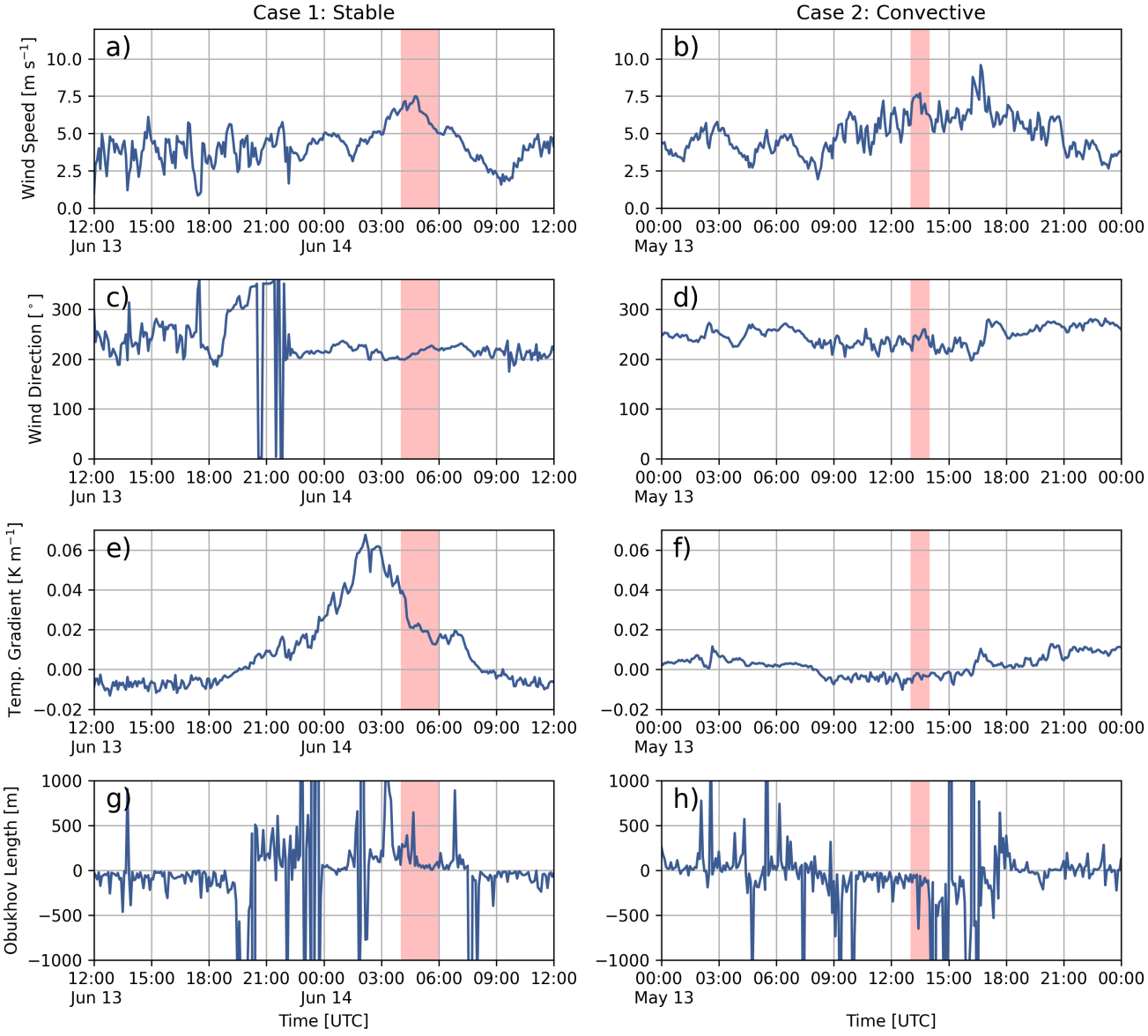

Figure 2. Hub-height (80 m) wind speed, wind direction, 100 m - 10 m potential temperature gradient, and Obukhov length for the stable case and for the convective case. Data are from SW_TSE04 and the periods of interest are highlighted in red. Data have been subsampled to five minute intervals.

2.2.2 Case 2: Convective Conditions

Typical daytime convective conditions on 13 May 2017 are indicated by the negative temperature gradient and Obukhov length in ~~Fig~~Figs. 2(f) and ~~Fig.~~ 2(h), respectively. For much of the day (08:00-16:00 UTC, 09:00-17:00 local time), the temperature

gradient is approximately -0.005 K m^{-1}. During the period of interest (13:00-14:00 UTC) ~~, and similar to the stable case study,~~ a wind speed of 7 m s^{-1} ~~will cause~~ causes the wind turbine to operate and generate wake effects. ~~Additionally, the wind direction is~~ The negative lapse rate results in an infinite internal Froude number and with wind perpendicular to the ~~ridges. During this period, neither the TLS nor any soundings were launched, therefore the met towers provide the main metric for quantitative validation.~~ ridge a turbulent mountain wake with recirculation should form.

3 Methods

3.1 WRF-LES-GAD

The present work utilizes the large-eddy simulation capability of the WRF model~~. The base source code is from~~ , version 3.7.1, with modifications including vertical grid nesting (Daniels et al., 2016), the generalized actuator disk (GAD) (Mirocha et al., 2014), and a turbine yawing capability (Arthur et al., 2020).

The GAD requires specifications for the turbine's airfoil lift and drag coefficients. The turbine located at the Perdigão site is a 2.0-MW E-82 Enercon turbine; however, the required lift and drag parameters are not publicly available. We therefore use the wind turbine parameterization from Arthur et al. (2020), which is similar but not identical to the turbine at Perdigão. Both turbine types have a roughly 80-m hub-height and rotor diameter, and are therefore expected to create similar wake effects. Minor differences between the two turbines are not expected to be critical to the conclusions of this study.

~~WRF-LES-GAD can be setup in a standalone LES-only configuration, or in a meso- to micro-scale (i.e., multi-scale) configuration. In the LES-only configuration, the wind speed, wind direction, surface heat flux, cooling rate, and various other environmental parameters can be set by the user. We refer to this as a semi-idealized setup.~~

3.2 ~~Semi-Idealized Simulation Setup~~

~~The three-dimensional semi-idealized setup uses a single domain with periodic boundary conditions. The grid resolution is 10 m and the two-dimensional terrain is derived from a cross-section of the Perdigão terrain which intersects the wind turbine and is perpendicular to the ridges (Wake Transect in Fig. 1). The two-dimensional terrain extends 2500 m in the span-wise direction and 5000 m in the streamwise direction. The domain height is just above 1400 m and Rayleigh damping is used within 500 m of the domain top with a coefficient of 0.003 s^{-1}. Two semi-idealized simulations are conducted, one to imitate the stable case study and the other to imitate the convective case study.~~

~~Streamwise velocity (u) normalized by the hub-height streamwise velocity (u_{hub}) for (a) the stable and (b) the convective semi-idealized setups.~~

~~For the stable semi-idealized simulation, the sounding launched on 14 June 2017 at 03:55 UTC in the valley at Perdigão is used to specify the geostrophic wind speed and potential temperature profile. The geostrophic wind direction is aligned with the x-axis, such that the forcing is entirely longitudinal. Additionally, a cooling rate of -0.25 K h^{-1} is used. The atmospheric boundary layer in the sounding is stably stratified with a low-level jet present. Short-term simulations (Fig. **??**(a)) capture the jet~~

deforming into a mountain wave after the first (southwest) ridge. Longer-term simulations are not possible as the stratification is eroded by turbulent mixing due to the periodic boundary conditions, which highlights the limitations of this semi-idealized setup.

For the convective semi-idealized simulation, we use a sounding with constant geostrophic wind speed (7 m s^{-1}) and potential temperature profiles. As in the stable case, the geostrophic wind direction is aligned with the x-axis. Convective conditions are prescribed using a uniform surface heat flux of 100 W m^{-2}. Initial simulations (not shown) showed that recirculation in the valley did not occur (Wise et al., 2020). Further investigation determined that recirculation did not occur due to the small surface roughness length, z_0, specified in the setup. Initially, we used $z_0 = 0.05$ m, which corresponds to the land use classification for much of the Perdigão site. The CORINE Land Cover data (Bossard et al., 2000) classifies much of the area as mixed shrubland/grassland which is transformed into United States Geological Survey (USGS) land use types to obtain surface roughness lengths (Pineda et al., 2004). Mixed shrubland/grassland equates to surface roughness lengths of 0.01 - 0.05 m (depending on the season). After setting the surface roughness length to 0.5 m, which is reasonable given the tall eucalyptus and fir trees covering most of the valley, recirculation, as defined by flow in the negative X-direction, did occur in the convective semi-idealized simulation (see Fig. **??**(b)). Wagner et al. (2019) similarly concluded that the surface roughness lengths at the Perdigão site based on the CORINE Land Cover data were too small.

3.2 Multi-Scale Simulation Setup

Having demonstrated the ability of WRF-LES-GAD to capture the different types of wake behavior in a semi-idealized setup, we now proceed to the full multi-scale simulation. A The 5-domain , nested multi-scale setup for WRF-LES-GAD (see is shown in Fig. 3, with details in Table 1) captures both mesoscale forcing and microscale features. The outermost domain, d01, captures mesoscale forcing and has a horizontal grid resolution of 6.75 km, and ; the innermost domain, d05, has a horizontal grid resolution of uses 10 m spacing and captures microscale flow features. The two coarsest domains are mesoscale simulations that use a planetary boundary layer (PBL) scheme, while the three inner domains use a microscale large-eddy simulation LES turbulence closure. There is a relatively large parent grid ratio of 15 from d02 to d03, intentionally chosen to skip across the gray zone where turbulence is only partially resolved (Wyngaard, 2004; Chow et al., 2019; Haupt et al., 2019; Muñoz-Esparza et al., 2017). The multi-scale setup also makes use of vertical grid nesting (Daniels et al., 2016) to adjust the terrain-following vertical resolution of vertical layers in each domain, with the grid spacing as fine as 8 m near the surface for d05 while and increasing for the coarser domains, up to roughly 60 m near the surface for d01. The coarser vertical resolution for d01 - d04 has the benefit of reducing computational costs (the current setup takes roughly eight hours of wall-clock time for five minutes of simulation time on 288 cores) while also maintaining an aspect ratio ($\Delta x/\Delta z$) closer to unity on the LES domains d03 and d04 (Daniels et al., 2016). On d05, most of the vertical resolution is devoted to the bottom ~2 km of the atmosphere, above which there is a gradual drop off in resolution all the way to the domain top of ~20 km. Because of the steepness of the terrain, numerical stability requires the use of very small time steps (as small as 1/60 s for d05). Domains d01, d02, and d03 were spun up for 9 hours, prior to starting d04, and d05. An overview of the nested-domain setup showing the geographical extent and topography of each of the domains is shown in Fig. 3.

Table 1. Parameters used for the nested multi-scale WRF-LES-GAD setup. For the vertical resolution, Δz_{min} is for the first grid point above the surface and is approximate due to the nature of the terrain-following coordinate system in WRF.

Domain	Δx [m]	Nest ratio	~Δz_{min} [m]	$N_x \times N_y$	Δt [s]	turb. closure
d01	6750	-	60	141 × 141	30	2.5-level MYNN
d02	2250	3	60	181 × 181	10	2.5-level MYNN
d03	150	15	30	271 × 271	0.5	TKE 1.5
d04	50	3	30	271 × 271	0.0833	TKE 1.5
d05	10	5	8	601 × 601	0.0167	TKE 1.5

All three LES domains (d03, d04, and d05) use a stochastic inflow perturbation method ~~known as (~~the cell perturbation method~~(;~~ CPM) to improve the downscaling of coherent, turbulent structures in the nested approach (Muñoz-Esparza et al., 2014, 2015) in a range of stability conditions (Muñoz-Esparza and Kosović, 2018). The CPM works by applying small temperature perturbations to the flow on the upwind domain boundaries that ~~lead to~~ accelerate the development of a full range of turbulent scales, at essentially no additional computational cost. While the use of high-resolution terrain data is expected to spur turbulence, Connolly et al. (2021) found that during convective conditions in the Perdigão valley, using the CPM further ~~improves~~ improved the representation of turbulence ~~. Additionally, they found that the CPM improves the~~ and the rate at which smaller-scale turbulence forms, with no known negative impacts on the flow from the perturbations. Similar findings regarding CPM are described by Arthur et al. (2020) for nested WRF-LES-GAD simulations of a wind farm in less complex terrain. ~~The CPM therefore allows us to reduce the spin-up time and fetch required for the high-resolution domains to develop realistic turbulent structures.~~

WRF-LES-GAD ~~uses~~ is run using a third-order Runge-Kutta time advancement scheme, with fifth-order horizontal and third-order vertical advection schemes. Relevant physical parameterizations selected include the Eta (Ferrier) scheme for microphysics (Rogers et al., 2001), the Noah land surface model (Chen and Dudhia, 2001), the Rapid Radiative Transfer Model for longwave radiation (Mlawer et al., 1997), and the Dudhia shortwave radiation model (Dudhia, 1989). The mesoscale simulations, d01 and d02, use the Mellor-Yamada–Nakanishi–Niino (MYNN) level-2.5 PBL scheme (Nakanishi and Niino, 2006, 2009), and d03, d04, and d05 use the turbulent kinetic energy (TKE) level-1.5 LES closure (Deardorff, 1980). All domains use the MYNN surface layer scheme ~~(Nakanishi and Niino, 2006, 2009)~~ in which the lower-boundary conditions are determined from Monin–Obukhov similarity theory. Additionally, topographic shading is enabled to account for shading effects on the surface heat flux in the complex Perdigão terrain. For the upper-boundary condition, we use a Rayleigh damping layer for the top 5 km of the domain.

~~We use~~ Mesoscale forcing for d01 is provided by Global Forecast System (GFS) data from the National Center for Environmental Protection (National Centers for Environmental Prediction, National Weather Service, NOAA, U.S. Department of Commerce, 2015)~~, made publicly available by the National Oceanic and Atmospheric Administration~~. In a sensitivity study

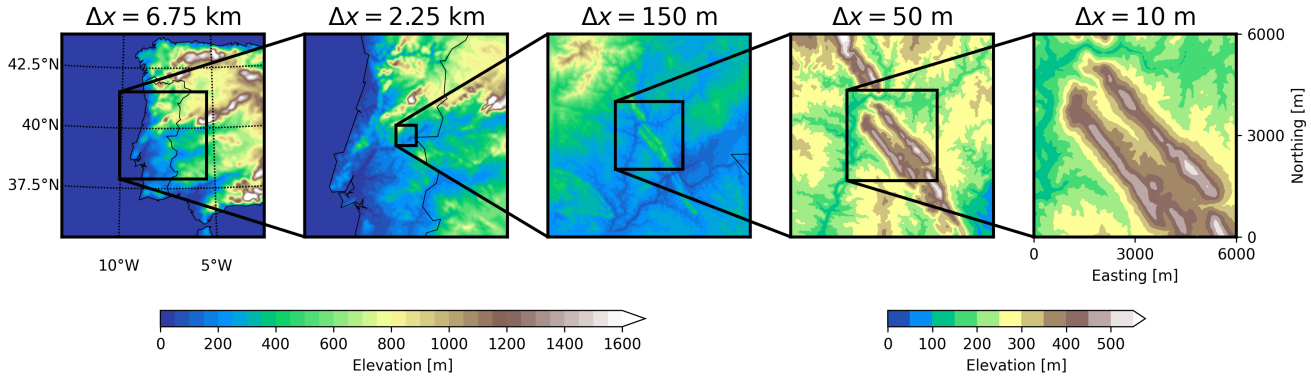

Figure 3. Topography of domains used in the multi-scale simulation centered over the Perdigão site. The five domains have resolutions of 6.75 km, 2.25 km, 150 m, 50 m, and 10 m. Dimensions of each domain and other configuration information are included in Table 1.

comparing both GFS and European Centre for Medium-Range Weather Forecasts data for the boundary conditions, the GFS data produced more accurate results near the surface for the dates of interest here (Wendels, 2019).

Land cover data was obtained from the Coordination of Information on the Environment (CORINE) dataset at a resolution of 100 m, much finer than the default land cover data provided ~~by NCAR for use~~ in WRF. The CORINE Land Cover 2006 raster dataset (Bossard et al., 2000) is transformed into United States Geological Survey (USGS) land use types to obtain surface roughness lengths for WRF (Pineda et al., 2004)~~, while~~ . The CORINE dataset seemingly misclassifies the land type in the valley as mixed shrubland/grassland when the vegetation is mostly tall eucalyptus and fir trees. Likewise, Wagner et al. (2019) concluded that the surface roughness ~~length of~~ lengths at the Perdigão site based on the CORINE Land Cover data were too small. To account for this, we set the surface roughness length for the mixed shrubland/grassland land use ~~index is manually set~~ category in the valley to 0.5 m~~. Additionally, high-resolution~~ , the same value used in the LES studies of Berg et al. (2017) and Dar et al. (2019). High-resolution terrain data (1-arc-second, approximately 30 m) were obtained from the Shuttle Radar Topography Mission (Farr et al., 2007). This high resolution terrain data is required to resolve flow features within the narrow valley (see Appendix A for more details).

4 Results and Discussion

4.1 Validation of the Stable Case Study

The stable case ~~selected on 14 June 2017, 04:00 - 06:00 UTC~~ is influenced by a mountain wave event. To ~~understand the scale of the mountain event , we can~~ validate the accuracy of this event in WRF-LES-GAD, we compare the model with multi-Doppler lidar scans obtained by the DTU lidars. The ~~lidars measure line-of-sight or radial velocities, so we project the~~ model u- and v-velocities ~~from the model~~ have been projected onto a rotated coordinate system aligned with the Wake Transect in Fig. 1 for comparison. ~~We use this transect to illustrate the wind turbine wake behavior. Note that this transect is oriented~~

~~approximately 48° from north. The lidars, however, are oriented~~ For the lidar, the line-of-sight velocities have been converted into horizontal velocity along the Offset Transect in Fig. 1~~, which is oriented approximately 49° from north. For the lidar, the~~. Velocity components perpendicular to the lidar's line-of-sight ~~velocities have been converted into just the horizontal component of the velocity. This results in a comparison of along-transect horizontal velocities between the model and the lidars shown in Fig. 4.~~

are not captured, so this conversion results in larger errors at higher elevation angles, but errors are small across the valley near the wind turbine, where the lidar beam is near horizontal. The wavelength of the mountain wave is defined as the distance from the first ridge (where the low-level jet begins to deform) to the first crest of the mountain wave. The model predicts ~~the wavelength of the mountain wave to be 1200~~a wavelength of 1220 m (Fig. 4(a)~~and Fig. 4(c)), which is slightly shorter than the 1500 m ridge-to-ridge distance at Perdigão. This prediction by the model is a slight underestimate of the measurements captured by the~~), 13% less than the 1410 m wavelength from the DTU lidars, ~~where the wavelength is closer to~~ which is almost exactly the ridge-to-ridge distance of 1400 m ~~; however, qualitatively, the model captures the mountain wave and associated turbulence quite well. The transects shown in Fig. 4 are nearly 7 km in length which is almost the entire extent of the computational domain. The~~ (Palma et al., 2020). In both the model and multi-Doppler lidar scans, the flow follows the terrain over each ridge, creating a small rotor in the Perdigão valley and a larger rotor beneath the third wave crest downstream of the valley. ~~Qualitatively, in both the model and multi-Doppler lidar scans, turbulent eddies are visible in the rotors with very little turbulence in the wave itself.~~

~~In~~

Figure 5 shows 1 h (from 04:30 to 05:30 UTC) time-averaged along-transect velocities for the stable case from the model and the DLR lidar scan along the Wake Transect (Fig. ~~4(a), the model also shows a small recirculation zone in the lee of the second ridge ($x \approx 1700$ m) which is not apparent in the multi-Doppler lidar scans of~~ 1). The lidar data are interpolated onto the model grid, and the difference between the model and observations is shown in Fig. ~~4(b); however, just a few minutes later in~~ 5(c). The height of the mountain wave does not extend as high in the model compared to measurements, likely a result of errors in the GFS forcing. This is clear in Fig. ~~4~~5(c)~~and Fig. 4(d), this recirculation zone is apparent in the multi-Doppler lidar scans but not~~ , where there are large differences in the along-transect velocity from roughly 800-1200 m a.s.l. The lidar data also show striations of slower and faster wind speeds within the wave, but these striations are not captured by the model. ~~These differences highlight the intermittent and dynamic nature of the phenomena of interest, even though the wind speed and wavelength of the mountain wave are relatively constant with time. Given the complexity of the flow, the overall qualitative agreement between the modeland the lidar observations is quite remarkable.~~ For both the model and the lidar scans, the wake propagates downward following the terrain into the valley. The velocity deficit from the turbine wake dissipates more quickly in the observations compared to the model. The model's resolvable turbulent length scale is limited by the grid resolution, making it possible that the model turbulence dissipation is underpredicted; in addition, this could be due to the different turbine model or errors from a number of other parameterizations.

~~The flow structure of the mountain wave captured by the model illustrated in Fig. 6 also agrees well with measurements from the TLS and met towers.~~

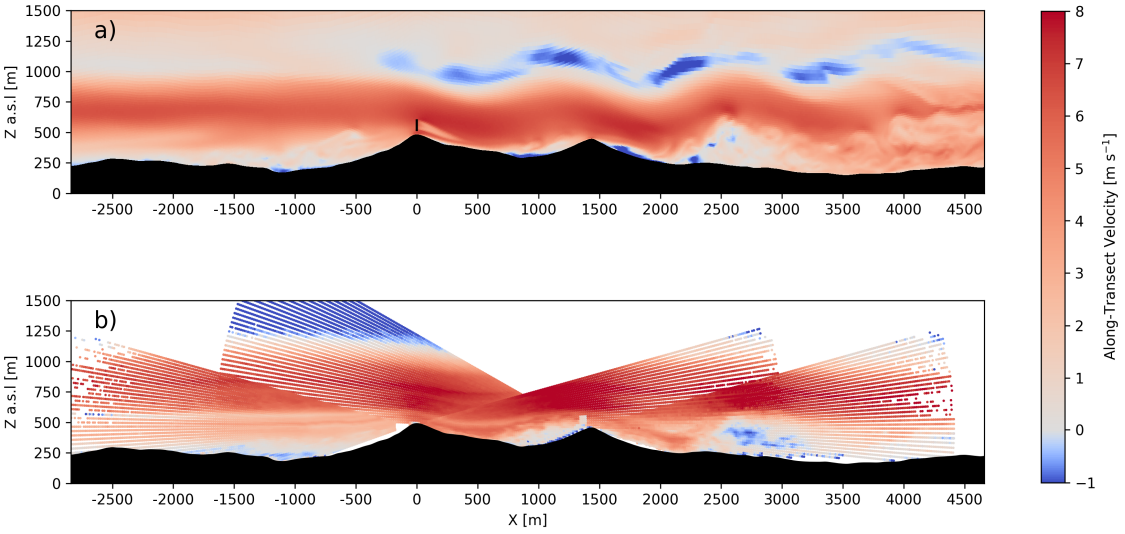

Figure 4. Instantaneous along-transect horizontal velocity during the stable case study for (a) the model and (b) the DTU multi-Doppler lidar scan at approximately 04:20 UTC. The output from the model is instantaneous while the multi-Doppler measurements are over the course of a single scan, which takes about 24 s. The model transects are aligned with the Wake Transect and the lidar transects are aligned with the Offset Transect in Fig. 1. An animation of model results during the entire two-hour period are included in the supplementary material (see Video 1, in the Video Supplement).

Figure 6 shows ~~the~~ instantaneous wind speed from the model overlaid with measurements from the TLS, and met towers V_TSE09 and NE_TSE13, at times when the TLS is near the surface, halfway up~~the ascent~~, near the top of its ascent, and halfway down its descent (the tower on the southwest ridge is omitted for clarity). ~~Additionally, in~~ Fig. 6~~,~~ (e) shows a time series from the model, a virtual TLS, ~~is~~ extracted using the GPS position at the corresponding time step of the actual TLS. Comparison of time-dependent turbulent flow fields from a model and a measurement system that moves in three-dimensions over time is difficult because the instantaneous positioning of turbulent flow features will likely not match. To partially account for this and for any uncertainty ~~in~~ of the TLS positioning ~~, time series with an easting and northing position~~ (estimated to be $\pm$30 m~~are shown in Fig. 6(e)but with a lighter shading. Additionally~~), the wind fields in Fig. 6(a-d) have also been spatially averaged by $\pm$30 m in the span-wise direction. Additionally, time series with an easting and northing position $\pm$30 m and $\pm$60 m are shown in Fig. 6(e) but with a lighter shading. During the two ascents, the virtual TLS and real TLS show good agreement with a root mean squared error (RMSE) under 2.0 m s^{-1}. However, the model slightly underestimates the strength of the jet and there is a negative bias of -0.78 m s^{-1} over the course of the two ascents and descents. ~~Between 04:30 - 04:45 UTC and 05:15 - 05:30 UTC, when the TLS is at its maximum in altitude, the model wind speed is 1-2 m s^{-1} lower than observations.During the descents of the TLS, the model decreases in wind speed slightly sooner, or at a higher altitude, compared to the actual TLS.~~

~~Instantaneous along-transect horizontal velocity during the stable case study for (a) the model and (b) the DTU multi-Doppler lidar scan at approximately 04:20 UTC, and for (c) the model and (d) the DTU multi-Doppler lidar scan at approximately 04:40 UTC. The output from the model is instantaneous while the multi-Doppler measurements are over the course of a single scan, which takes about 24 s. The model transects are aligned with the Wake Transect and the lidar transects are aligned with the Offset Transect in Fig. 1. An animation of model results during the entire two-hour period are included in the supplementary material (see Video 1, in the Video Supplement).~~

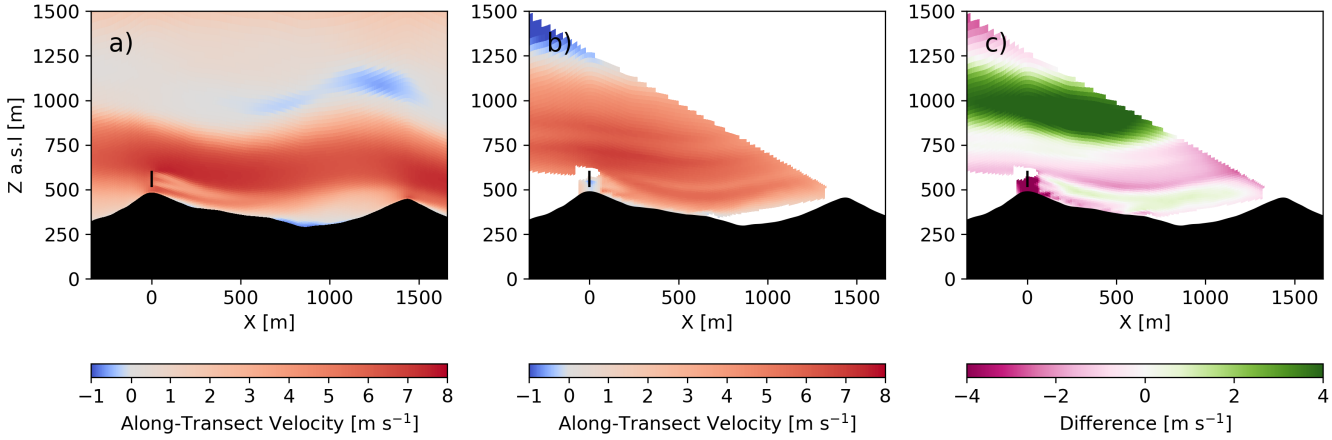

Figure 5. Transect of 1 h time-averaged along-transect velocity for the (a) model and (b) DLR lidar during the stable case study with (c) as the difference between the DLR lidar and the model. The transects are aligned with the Wake Transect in Fig. 1.

~~Given the challenges in such a comparison, the overall agreement between the TLS and~~ In Fig. 6(e), the predictions for ±30 m and ±60 m are similar because the flow is relatively homogeneous in the spanwise direction (a result of the ~~model output is notable.~~

~~The 10-m and 80-m data points on the met tower in the valley indicate decreased shear compared to the met tower on the downstream ridge. The model predicts that the 10-m and 80-m locations for V_TSE09 are located below the mountain wave and in a region of more well-mixed and coherent turbulence. The TLS rises above the region of well-mixed turbulence and into the mountain wave. There is a small underestimation in wind speed of 1 to 2 m s^{-1} when the TLS is near the top of its ascent. Near-surface wind speeds on the downstream ridge show some discrepancies (sometimes on the order of 3 to 4 m s^{-1}). Note, however, that exact agreement is not expected in these instantaneous snapshots.~~

~~Figure 6 also shows that the wind turbine wake, while time-varying, is deflected by the mountain wave into the valley. The wake likely then meanders out of the transect since the transect and wind direction are slightly misaligned, and also because the wake veers (~~limited terrain variability in this direction, as seen in Fig. 11 and discussed more in ~~Sect.~~Section 4.3). ~~The transects still indicate that the wind turbine wake can propagate at least 800 m downstream, or close to 10 rotor diameters.~~

Wind speed, wind direction, and the potential temperature gradient are also compared with met tower measurements in Fig. 7. The modeled wind speed and wind direction generally follow the observations at both hub-height (80 m) and near the surface (10 m), with greater variability in the valley compared to on top of the two ridges. ~~The 100 m - 10 m potential temperature gradient also compares favorably with measurements but with a longer duration of agreement on top of the two~~

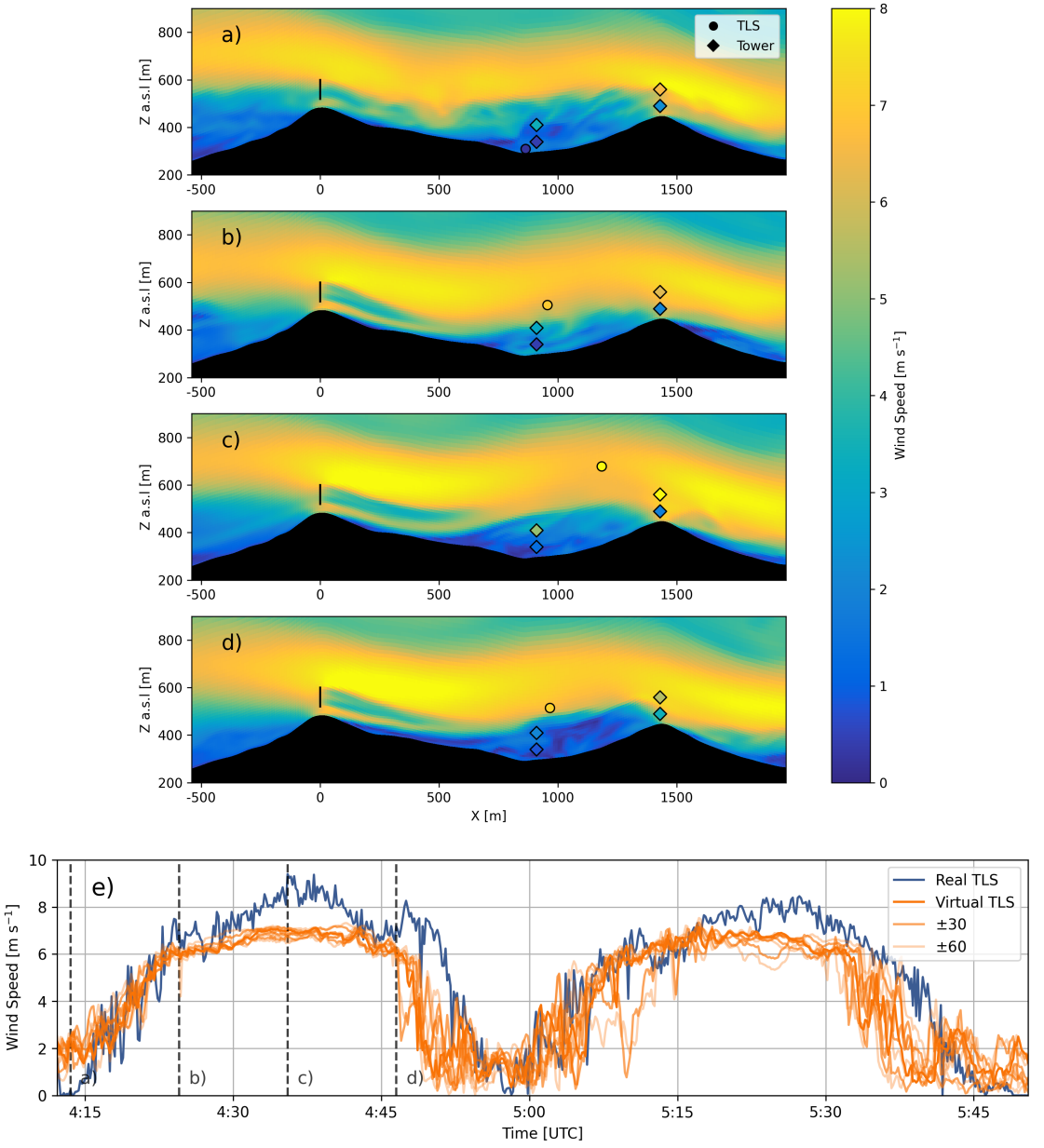

Figure 6. Transects of instantaneous wind speed for WRF with measurements from V_TSE09, NE_TSE13, and the TLS overlaid for (a) 04:13:30 UTC, (b) 04:24:30 UTC, (c) 04:35:30 UTC, and (d) 04:46:30 UTC and (e) comparison of wind speed between the TLS data and the virtual TLS in WRF-LES-GAD d05. The transects are aligned with the Wake Transect in Fig. 1. Virtual TLSs with an easting and northing position ±30 m and ±60 m are shown with a lighter shading and dashed lines indicate the times shown in the transects. An animation of model results for when the TLS is operational is included in the supplementary material (see Video 2, in the Video Supplement).

Table 2. Wind speed, wind direction, and temperature gradient ~~biases~~ bias and ~~errors~~ RMSE between WRF-LES-GAD and meteorological tower measurements for the stable case study.

	SW_TSE04		V_TSE09		NE_TSE13	
Parameter	Bias	RMSE	Bias	RMSE	Bias	RMSE
80 m Wind Speed (m s^{-1})	-0.22	0.83	-0.51	2.01	-0.69	1.34
10 m Wind Speed (m s^{-1})	-0.48	0.81	0.98	1.25	2.65	2.90
80 m Wind Direction (°)	-0.4	8.4	-12.7	64.1	0.0	11.3
10 m Wind Direction (°)	-8.1	18.5	-28.9	120.5	-0.2	19.0
Temperature Gradient (K m^{-1})	-0.003	0.011	-0.014	0.017	0.004	0.007

~~ridges relative to the valley. Figure 7 compares the 80 m wind speed and wind direction and the temperature gradient between the met towers and the model. The model wind speed and direction are output at 10 s intervals while the temperature is output every 150 s. Also note that the three towers lie along the Offset Transect in Fig. 1.~~

Errors quantified in terms of bias and RMSE are shown in Table 2. At hub-height and along the two ridges, wind speed errors are below 1.5 m s^{-1} and wind direction errors are below 12°. ~~The variability in the inflow can be quantified by the standard deviation which is 0.95 m s^{-1} for the model and 0.72 m s^{-1} for SW_TSE04.~~ Within the valley, ~~the wind speed and wind direction agree well with measurements from V_TSE09, but less so compared to the measurements at the top of the ridges, with~~ hub-height wind speed and wind direction errors are on the order of 2 m s^{-1} and 60°, respectively. Both the wind speed and wind direction fluctuate much more in the valley compared to the ridges, which the model captures ~~fairly~~ reasonably well considering the low wind speeds present. The temperature gradient within the valley in the model is indicative of a well-mixed region whereas the measurements indicate more stable stratification, resulting in an RMSE of 0.017 K m^{-1}, although this stratification does vary significantly over the period of interest. This discrepancy is also evident in Fig 6(a-d) where the model predicts that the 10-m and 80-m locations for V_TSE09 are located below the mountain wave and in a region of more well-mixed and coherent turbulence.

~~The vertical structure of the flow is investigated next by comparing the model with two soundings in Fig. **??**. The first sounding was launched five minutes prior to the analysis period, but obtained data into the period of interest therefore providing a useful comparison. Figure **??** shows the wind speed, wind direction, and potential temperature for the soundings launched at 03:55 and 05:16 UTC and the innermost domain of the model, up to 5000 m above the surface. Errors in terms of bias and RMSE between the soundings and the model are shown in Table **??**.~~

4.2 Validation of the Convective Case Study

~~For the first sounding, overall wind speed errors are small, with a bias of -0.52 m s^{-1} and RMSE under 2 m s^{-1}; however, as previously observed when comparing the model with measurements, the strength of the jet is underestimated. Using the velocity at the nose of the jet, which is at 650 m a.s.l. in the model and 720 m a.s.l in the observations, we can calculate a~~

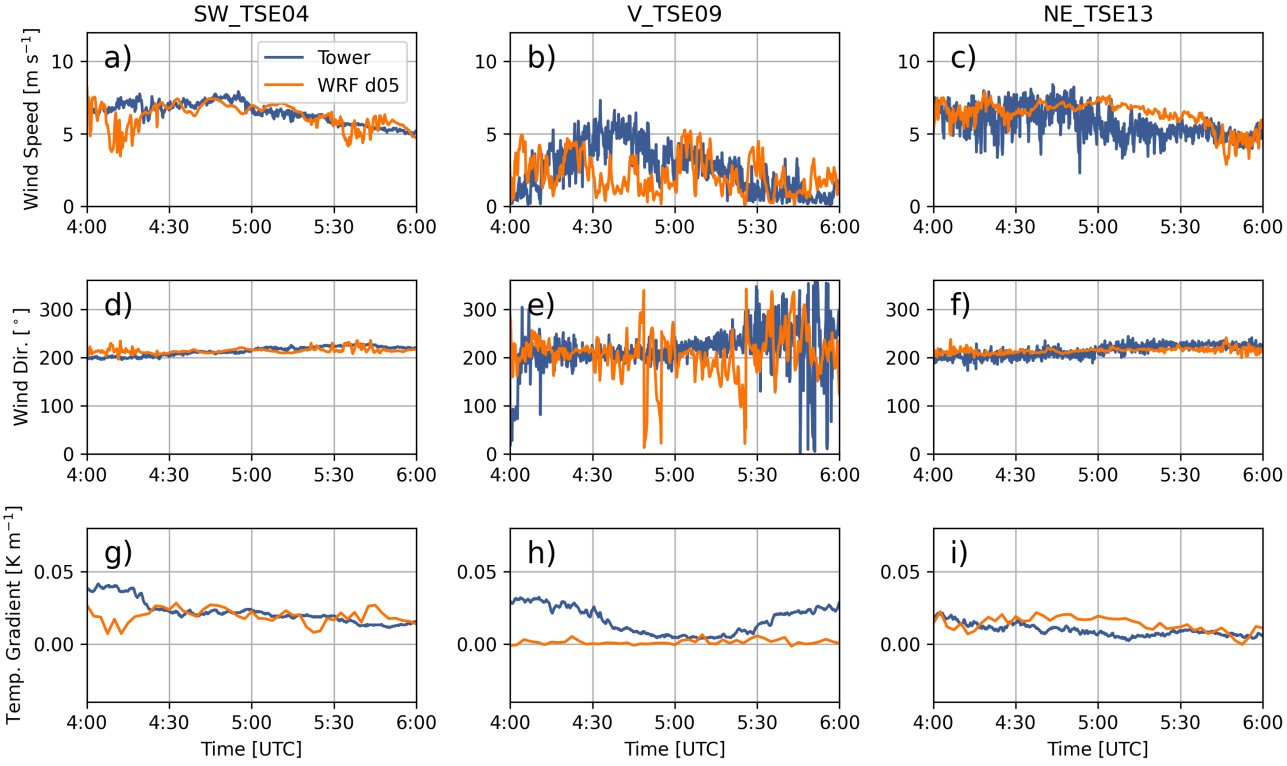

Figure 7. Comparison between meteorological tower data and WRF-LES-GAD d05 for 80 m wind speed (a-c), 80 m wind direction (d-f) and 100 m - 10 m temperature gradient (g-i) for the stable case study. SW_TSE04 and NE_TSE13 are located on ridges while V_TSE09 is located in the valley. Note that the model wind speed and direction are output at 10 s intervals while the temperature is output every 150 s.

~~Froude number at the beginning of the period of interest. The Brunt-Väisälä frequency can be estimated as 0.035 s^{-1} (see Fig. **??**) and the mountain height is approximately 230 m. Using a free stream wind speed $U = 9.8$ m s^{-1} for the sounding and 7.1 m s^{-1} for the model, the Froude numbers are 1.2 and 0.9, respectively. The lower Froude number for the model results in a shorter wavelength for the mountain wave, as was seen in Fig. 4. The model struggles to capture the near-surface wind direction in the valley, however this is primarily because wind direction is sensitive to fluctuations at lower wind speeds. The wind direction also deviates between 1-2 km above sea level (a.s.l) but the overall errors are small with a bias of 2.2° with very strong agreement in the upper atmosphere. There is a small negative bias for the potential temperature on the order of -0.3 K, but the height of the stable layer is accurately captured by the model with an inversion located close to 600 m a.s.l. For the second sounding, overall wind speed errors are similarly small, although a ~2 m s^{-1} decrease in wind speed within the nose of the jet is observed in the sounding at about 800 m a.s.l. This decrease in wind speed could be the turbine wake or the striation of lower wind speed seen close to 600 m a.s.l in the~~ As for the stable case, WRF-LES-GAD is validated for the convective case using comparisons to the multi-Doppler lidar scans ~~from the beginning of the transect until the rotor in the lee~~

of the second ridge at X = 2500 m (Fig. 4(b)and Fig. 4(d)). This decrease in wind speed does not emerge in the model. Similar to the first sounding, the wind direction deviates near the surface and between 1-2 km a.s.l during the second sounding, but is largely captured aloft. The small negative bias of -0.3 K for potential temperature is also apparent for the second sounding, but the height of temperature inversion is accurately captured close to 600 m a.s.l or 300 m above the valley floor.

Comparison between the two sounding launched during the stable case study and WRF-LES-GAD d05 for wind speed, wind direction, and potential temperature.

Wind speed, wind direction, and potential temperature biases and errors between WRF-LES-GAD d05 and soundings for the stable case study. l | c c | c c Parameter Bias RMSE Bias RMSE Wind Speed (m s^{-1}) -0.52 1.58 0.77 2.34 Wind Direction (°) 2.2 32.9 -4.6 36.6 Potential Temperature (K) -0.35 1.11 -0.29 1.27

As seen in Fig. 5, time-averaged velocities highlight that the model predicts the overall characteristics of the flow and wind turbine wake behavior accurately when compared with lidar scans; however, there are minor discrepancies associated with the height and wavelength of the mountain wave as well as with the flow within the wave. Figure 5 shows 1 h (from 04:30 to 05:30 UTC) time-averaged velocities for the stable case from the model and the DLR lidar scan along the Wake Transect (Fig. 1). The velocities from the model and DLR lidar have been projected along-transect as in Fig. 4. As mentioned in the previous section when looking at the soundings, the height of the mountain wave does not extend as high in the model compared to measurements. This is clear in Fig. 5, where the height of the wave ends close to 1200 m when there is flow in the opposite direction. For the model, the height of the wave ends closer to 900 m. The lidar data also show striations of slower and faster wind speeds within the wave, but these striations are not captured by the model. For both the model and the lidar scans, the wake propagates downward following the terrain into the valley. The velocity deficit dissipates more quickly in the observations compared to the model. The model's resolvable turbulent length scale is limited by the grid resolution, and for stable boundary layers this length scale can be small. It is possible that turbulence dissipation for the model is under predicted and this could be due to the different turbine model or due to errors from a number of other parameterizations.

Transect of 1 h time-averaged along-transect velocity for the model (a) and DLR lidar (b) during the stable case study.

4.3 Convective Case Study

The convective case on 13 May 2017, 13:00 - 14:00 UTC is much more turbulent compared to the stable case due to surface heating. Increased turbulent mixing and unstable stratification 8). Unstable stratification and increased turbulent mixing lead to a turbulent mountain wake in the lee of the first ridge, which forms a recirculation zone . WRF-LES-GAD and the multi-Doppler lidar scans can be similarly compared for the convective case as they were for the stable case (as seen in Fig. 4). Reverse flow 8. Reverse flow or recirculation near the surface in the lee of the first ridge is both predicted by the model and observed by the multi-Doppler lidar scansas seen in Fig. 8. Turbulent eddies are clearly . Additionally, turbulent eddies are visible over the entirety of the transects in Fig. 8(a) and Fig. 8(b).

As seen The wind turbine wake interaction with the recirculation zone is shown in Fig. **??**, the flow inside the valley and near the two ridges is highly dynamic but very accurately predicted by WRF-LES-GAD. Figure **??** shows the instantaneous wind speed from the model overlaid with measurements from V_TSE09 and NE_TSE13 at four different instances. A similar

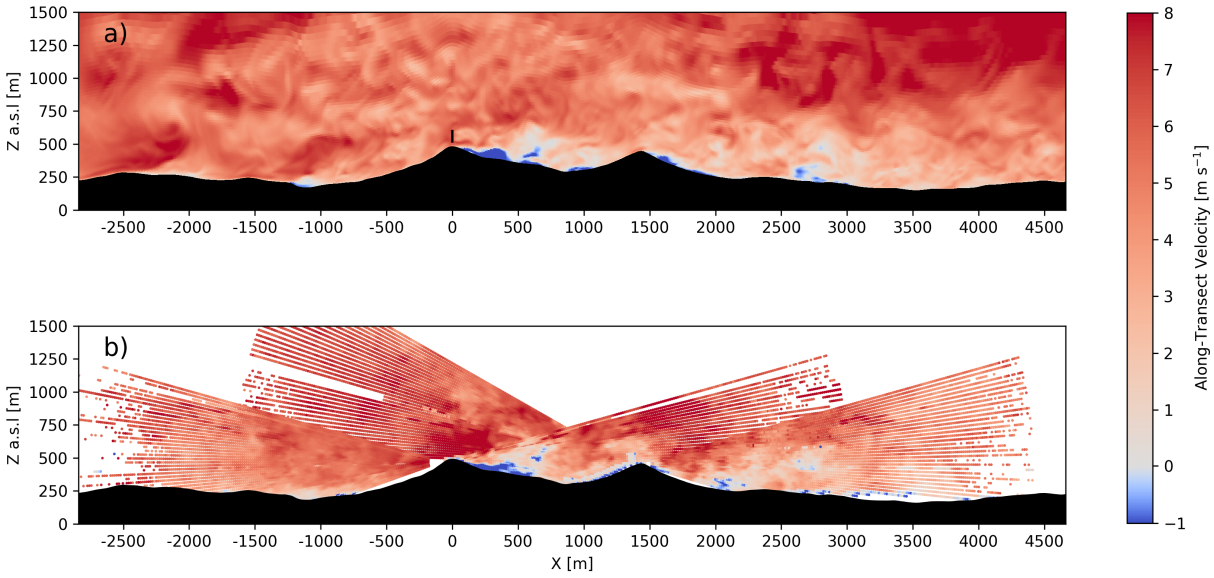

Figure 8. Instantaneous along-transect horizontal velocity during the convective case study for the model (a) and DTU multi-Doppler lidar scan (b) at approximately 13:20 UTC. The output from the model is instantaneous while the multi-Doppler measurements are over the course of a single scan, which takes about 24 s. The model transect is aligned with the Wake Transect and the lidar transect is aligned with the Offset Transect in Fig. 1. An animation of model results during the entire one-hour period are included in the supplementary material (see Video 3, in the Video Supplement).

~~procedure as for Fig. 6 is followed here for~~ 9 over a 1 h time average (from 13:00 to 14:00 UTC). From Fig. 9, the recirculation zone in the lee of the first ridge extends nearly 500 m into the valley for both the model and the lidar measurements as indicated by the small difference in velocities (< 1 m s^{-1}) in Fig. **??**. ~~Note that the TLS was not operational during the convective case study and is therefore not available for comparison. Wind speeds are very slow in the lee of the first ridge, representing a mountain wake . Above this mountain wake, there is a strong shear layer with higher wind speeds in which the~~ 9(c). In both the model and measurements, the wake does not mix with the recirculation zone or mountain wake and deflects upwards; however, the model predicts faster velocities below the wind turbine wake ~~propagates. While the flow is both dynamic and highly turbulent, measurements from V_TSE09 show slow wind speeds both near the surface and at 80 m during all four instances. This indicates that V_TSE09 is generally within the mountain wake of the first ridge. Wind speeds at 80 m for NE_TSE13 are higher than wind speeds near the surface at all four time instances, which the model generally, but not always agrees with.~~ and above the recirculation zone.

~~The wind speed and wind direction are well-captured by the model on the ridges but with larger discrepancies in the valley as illustrated by~~

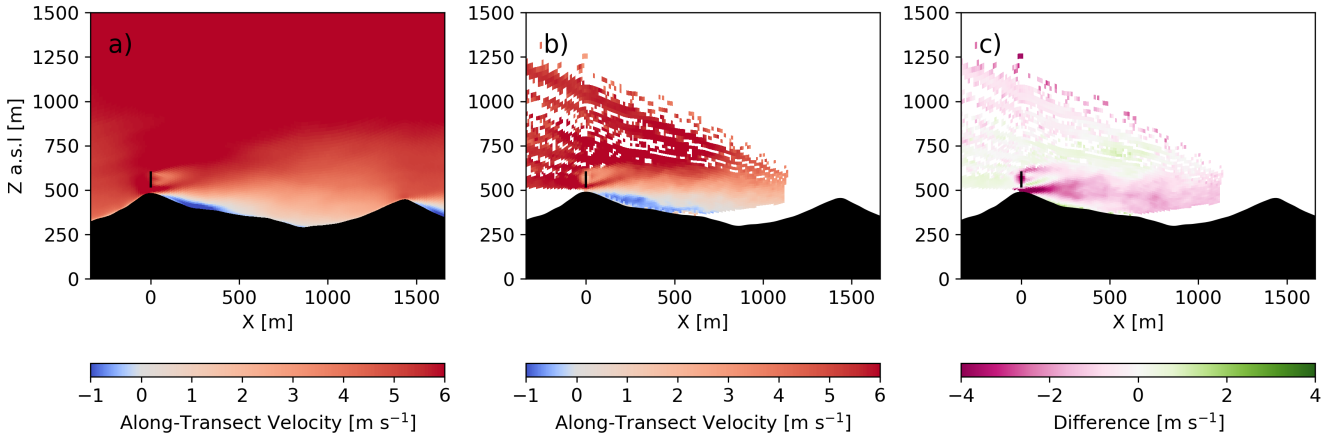

Figure 9. ~~Transects~~ Transect of ~~instantaneous wind speed~~ 1 h time-averaged along-transect velocity for ~~WRF with measurements from V_TSE09 and NE_TSE13 for~~ the model (a) ~~13:13:30 UTC,~~ and DLR lidar (b) ~~13:24:30 UTC,~~ during the convective case study with (c) ~~13:35:30 UTC,~~ as the difference between the DLR lidar and ~~(d) 13:46:30 UTC~~the model. The transects are aligned with the Wake Transect in Fig. 1.~~An animation of model results during the entire one-hour period are included in the supplementary material (see Video 4, in the Video Supplement).~~

A comparison with WRF-LES-GAD and the meteorological towers in Fig. 10 ~~. Additionally, there is more variability in the potential temperature gradient for the model compared with observations. Figure 10 shows the 80 m wind speed~~and during this time period, shows all three parameters (wind speed, wind direction, and ~~the 100 m - 10 m potential temperature gradient for the model as compared with the towers on the southwest ridge, in the valley, and on the northeast ridge. During this time period, all three metrics~~ temperature gradient) are relatively constant with the greatest variability in the wind speed and wind direction in the valley. ~~Overall, the fluctuations in measurements are much more pronounced in this convective case compared to the stable case (Fig. 7). Variability in the inflow is slightly over-predicted with a standard deviation over the hour-long period of 1.74 m s^{-1} for the model and 1.16 m s^{-1} for SW_TSE04.~~

Errors between the model and the met tower measurements at both 80 m and 10 m are shown in terms of bias and RMSE in Table 3~~. During the period of interest,~~ , with wind speed errors ~~are roughly 2~~less than 2.5 m s^{-1}~~or less~~. Larger errors in the near-surface wind direction within the valley are a result of lower wind speeds and increased turbulence, as compared to the flow on the ridges. Despite the variability in the modeled temperature gradient (Fig. 10g-i), the bias and RMSE values are small relative to the magnitude of the gradient itself~~, indicating that the average strength of thermal stratification is captured well throughout the period of interest.~~ .

~~While no sounding was launched during the convective period of interest, a sounding was launched on 13 May 2017 at 11:15 UTC. Domains d04 and d05 are not launched until after this time, but d03 has been running for over eight hours at this point. Figure **??** compares the wind speed, wind direction, and potential temperature profiles from WRF-LES-GAD d03 and those obtained by the sounding. In Fig. **??**, there are two soundings for the model, one sounding virtually launched at the~~

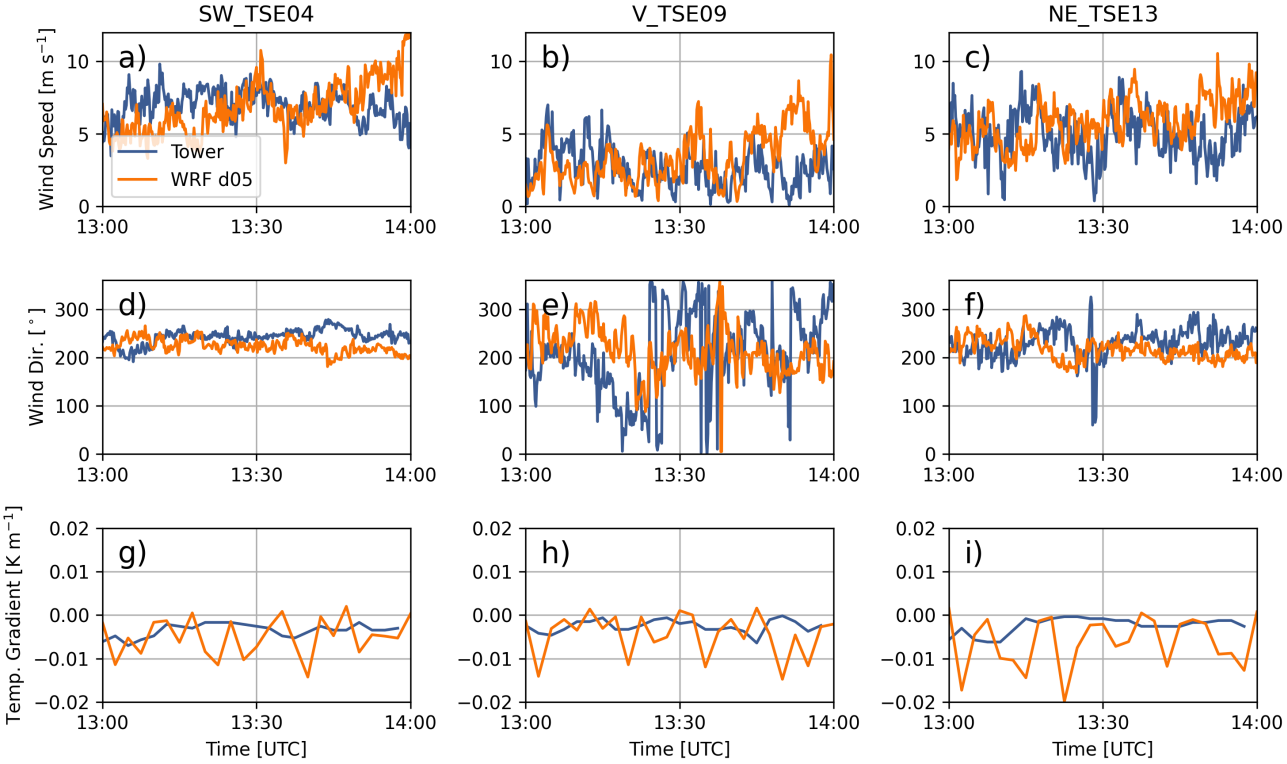

Figure 10. Comparison between meteorological tower data and WRF-LES-GAD d05 for 80 m wind speed (a-c), 80 m wind direction (d-f) and 100 m - 10 m temperature gradient (g-i) for the convective case study. SW_TSE04 and NE_TSE13 are located on ridges while V_TSE09 is located in the valley. Note that the model wind speed and direction are output at 10 s intervals while the temperature is output every 150 s.

Table 3. Wind speed, wind direction, and temperature gradient ~~biases~~ bias and ~~errors~~ RMSE between WRF-LES-GAD and meteorological tower measurements for the convective case study.

	SW_TSE04		V_TSE09		NE_TSE13	
Parameter	Bias	RMSE	Bias	RMSE	Bias	RMSE
80 m Wind Speed (m s^{-1})	~~1.70~~ -0.20	2.17	0.62	2.38	-0.74	2.04
10 m Wind Speed (m s^{-1})	-0.12	2.25	1.28	2.12	0.35	1.67
80 m Wind Direction (°)	-19.5	31.6	6.4	101.2	-14.5	44.0
10 m Wind Direction (°)	-15.5	23.9	77.1	141.2	-13.3	39.2
Temperature Gradient (K m^{-1})	-0.002	0.005	-0.002	0.005	-0.004	0.007

~~same time as the real sounding (11:15 UTC) and another sounding virtually launched an hour later (12:15 UTC). The potential temperature profile for the first sounding in the model is under predicted by close to 2 K in the lower atmosphere; however,~~

the potential temperature profile in the second sounding from the model is well-mixed and matches the observed temperature profile much better. The RMSE for potential temperature is half of that for the second sounding compared to that of the first sounding (see Table **??**). This indicates that there is a short delay in the model when capturing the thermal evolution of the atmosphere. The wind speed and wind direction profiles show strong agreement for both soundings, especially in the upper atmosphere. The wind speed biases are less than 1 m s^{-1}; however, the RMSEs are closer to 2 m s^{-1} indicating less variability in the model. This lack of variability is not unexpected for d03 because the grid resolution is only 150 m.

Comparison between the sounding, launched at 11:15 UTC, and soundings virtually launched (VL) in WRF-LES-GAD d03 for wind speed, wind direction, and potential temperature. WRF - d03 VL1 corresponds to a virtually launched sounding at 11:15 UTC and WRF - d03 VL2 corresponds to a virtually launched sounding at 12:15 UTC.

Wind speed, wind direction, and potential temperature biases and errors between WRF-LES-GAD d03 and sounding for the convective case study. l | c c | c cParameter Bias RMSE Bias RMSE Wind Speed (m s^{-1}) 0.80 1.66 0.87 1.87 Wind Direction (°) 1.17 10.42 -6.99 14.78 Potential Temperature (K) -0.24 1.07 -0.17 0.51

The time-averaged velocities in Fig. 5 demonstrate that the recirculation zone in the lee of the first ridge is very well predicted in terms of size, and that the wind turbine wake, in general, deflects above this recirculation zone. We can similarly compare the model with the DLR lidar, as was done for the stable case (Fig. 5), to characterize the wind turbine wake interaction with the recirculation zone. This comparison is shown in Fig. 9 over a 1 h time average (from 13:00 to 14:00 UTC). We define recirculation as flow (along-transect horizontal velocity) in the upwind or negative direction. From Fig. 9, we can see the recirculation zone in the lee of the first ridge, which extends nearly 500 m into the valley for both the model and the measurements by the lidar. Additionally, there is also an area of slower wind speeds above the recirculation zone that can be classified as a mountain or ridge wake. For both the model and measurements, the wake does not mix with the recirculation zone or mountain wake and deflects upwards.

Transect of 1 h time-averaged along-transect velocity for the model (a) and DLR lidar (b) during the convective case study. The transects are aligned with the Wake Transect in Fig. 1.

4.3 Wind Turbine Wake Behavior

For the complex Perdigão terrain, Menke et al. (2018) and Wildmann et al. (2019) showed that wind turbine wakes in stable stratification can be observed up to 10 rotor diameters (D) downstream, following the terrain into the valley. Our model agrees with these observations. Figure 11 shows instantaneous 1 h time-averaged wind speed at approximately 80 m above the terrain for the stable case (14 June 2017 04:3730-05:30 UTC) and the convective case (13 May 2017 13:33:20 00-14:00 UTC). We can see the The wake signature in terms of a wind speed deficit persisting persists over 700 m into the valley for the stable case. The wake for the convective case dissipates much more quickly; however, this terrain-following plan-view makes it difficult to visualize the wake's extent because the wake deflects upwards in the convective case. .

The entirety of the wake cannot be visualized in two-dimensions because of wind veer and horizontal/vertical meandering. Three-dimensional visualizations provide insight into the wind turbine wake advection, meandering, and direction downstream as the flow evolves and develops over the first ridge and through the valley. Figure 12(a) and Fig. 12(b) show a volume rendering

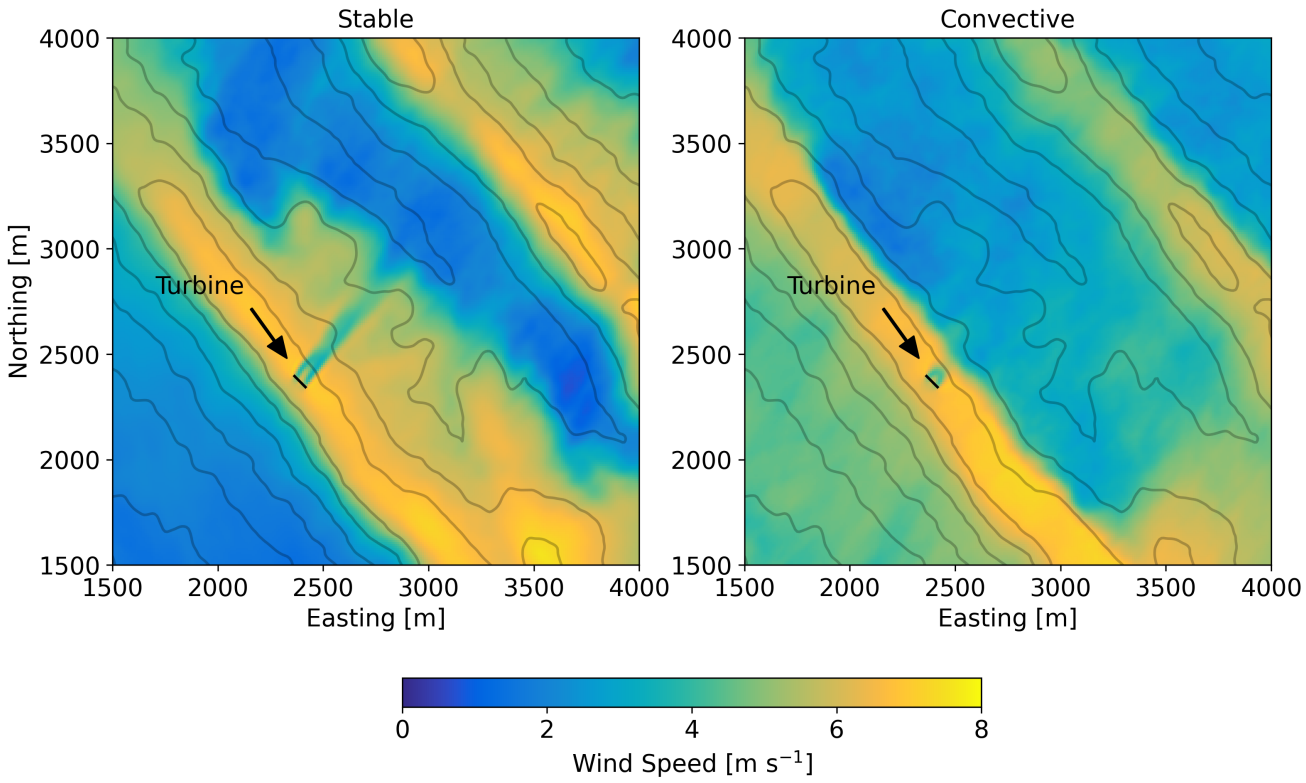

Figure 11. ~~Instantaneous~~ 1 h time-averaged wind speed contours at 80 m above the terrain for the stable case study ~~at 14 June 2017 04:37:30 UTC~~ and for the convective case study~~at 13 May 2017 13:33:20 UTC~~. ~~Contours~~ Line contours represent 50 m changes in elevation.

of wind speed at 04:37:30 UTC for the stable case. Note that the colorbar has been designed to highlight the velocity deficit imparted by the wind turbine rotor. ~~We can see in~~ In Fig. 12(a)~~that~~ , the coherent, tubular structure that is the wind turbine wake propagates downward into the valley following the terrain. At wind speeds highlighted by the volume rendering, the wind turbine wake is the dominant structure compared to any background turbulence in the flow field. In Fig. 12(a), the wake persists well into the valley and only begins to dissipate as it reaches the second ridge. Figure 12(b) shows how the wake meanders as it propagates into the valley. Wind veer causes the wake to deflect to the north near the second ridge.

Turbulent structures dominate the flow field in the convective case. A volume rendering of wind speed at 13:33:20 UTC for the convective case is shown in Fig. 12(c) and Fig. 12(d). A similar design of the colorbar that was done for Fig. 12(a) and Fig. 12(b) is done here for Fig. 12(c) and Fig. 12(d) except that the visible range of wind speeds is shifted from 3.0-5.0 m s^{-1} to 3.5-5.5 m s^{-1}. Additionally, data to the south and west of the wind turbine have been omitted for clarity. The wake structure is not nearly as coherent and dissipates much more quickly in the convective case compared to the stable case. Figure 12(c) clearly shows the wake as the dominant feature on top of the first ridge. Directly behind the rotor, the wake is level but is then deflected upwards. Background turbulence begins to dominate in the lee of the first ridge and into the valley. The ~~camera~~

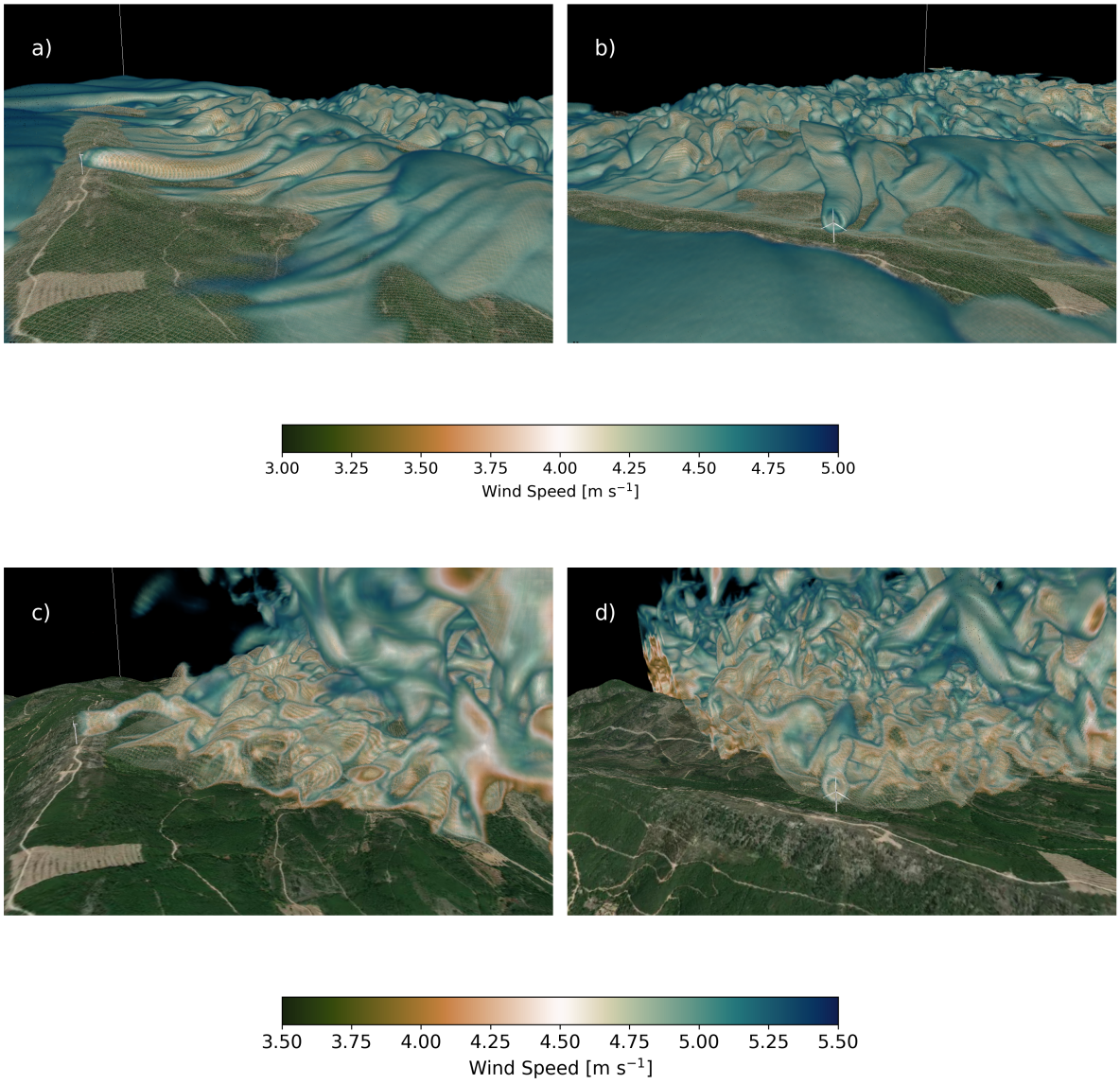

Figure 12. Three-dimensional volume ~~render~~ rendering of wind speed for the stable case at 04:37:30 UTC (a and b) and for the convective case at 13:33:20 UTC (c and d). For the stable case, only wind speeds between 3.0 and 5.0 m s^{-1} are shown and the wind speeds at the first five vertical levels have been removed for clarity. For the convective case, only wind speeds between 3.5 and 5.5 m s^{-1} are shown and data to the south and west of the turbine have been removed for clarity. The view point in (a) and (c) is from the southeast looking down the valley to the northwest. The view point in (b) and (d) is southwest of the wind turbine looking to the northeast. Visualization made using VAPOR (Clyne et al., 2007).

viewing angle used in Fig. 12(d) makes it so the wake is difficult to distinguish from any background turbulence except very close to the rotor.

The recirculation zone for the convective case and the mountain wave for the stable case modulate the flow behavior in the valley. The evolution of these phenomena, their interaction with the wind turbine wake, and any spatial heterogeneity in the flow can be visualized using $y-z$ cross sections of the wake at different downstream distances. Figure 13 shows 1 h time-averaged wind speed for the two stability cases at distances of 1D, 2D, 3D, and 4D along the Wake Transect (see Fig. 1). For the stable case, the wake propagates downward, following the terrain, above the slower near-surface winds. Additionally, the upper half of the wake veers in the positive y-direction leading to an ellipsoid shape for the wake. This stretching of the wake due to the veer in the inflow is characteristic of stable conditions (Lundquist et al., 2015; Abkar et al., 2016; Bromm et al., 2017; Churchfield and Sirnivas, , while the amount of veer in the wake depends on the shape and magnitude of the inflow veer (Englberger and Lundquist, 2020) . For the convective case, we ~~can~~ see that as the flow follows the terrain down into the valley, the recirculation zone and mountain wake rise in height. The wake structure is circular and much more coherent at distances of 1D and 2D compared to further downstream; however, a wind speed deficit is still clearly visible above the recirculation zone further downstream. The wake also drifts slightly in the positive ~~Y-direction~~y-direction, but this is due to the slight misalignment between the Wake Transect and the mean wind direction. ~~For the stable case, the wake propagates downward, following the terrain, above the slower near-surface winds. Additionally, we see the upper half of the wake veer in the positive Y-direction leading to an ellipsoid shape for the wake. This stretching of the wake due to the veer in the inflow is characteristic of stable conditions (Lundquist et al., 2015; Abkar et al., 2016; Bromm et al., 2017; Churchfield and Sirnivas, 2018; Englberger and Dörnbrack, 20 , while the amount of veer in the wake depends on the shape and magnitude of the inflow veer (Englberger and Lundquist, 2020)~~ .

To further quantify wake behavior in the Perdigão terrain, we determine the wake center locations downstream of the wind turbine. Using the model data, we extract 1 h time-averaged velocity profiles at distances of ~~-2D, -1D, 0D,~~ 1D, 2D, 3D, and 4D from the rotor along the Wake Transect. ~~Since the terrain is similar on parallel transects, we~~ We also extract 1 h time-averaged velocity profiles ~~at a lateral distance of 150 m parallel to the Wake Transectat the same locations upstream and downstream of the turbine. These velocity profiles 150 m further away do not capture the wake velocity deficit while the profiles directly behind the rotor do. The~~ along the Offset Transect. Since the terrain is similar on the nearly parallel transects, the velocity deficit can ~~then~~ be calculated by taking the difference between the profiles ~~150 m further away~~ along the Offset Transect and the profiles ~~that include the turbine wake. This difference results in a positive velocity deficit for the wake. The~~ along the Wake Transect. We follow a similar procedure with the observations. The DLR lidar represents the velocity profiles along the Wake Transect while the DTU lidar represents the velocity profiles along the Offset Transect. In these velocity deficit profiles, the vertical wake centers can then be determined by finding the vertical location at which the velocity deficit ~~profile~~ is greatest.

~~The velocity deficit profiles show that the wake tracks upwards in the convective case and follows the terrain for~~ In Fig. 14, the vertical wake centers follow similar patterns between the measurements and model with the wake centers tracking downwards in the stable case ~~(Fig. **??**). The wake deflects upwards above the hub-height by 11 m 1D downstream and up to as high as 54 m for 4D downstream for the~~ and upwards in the convective case. For the stable case, the wake deflects

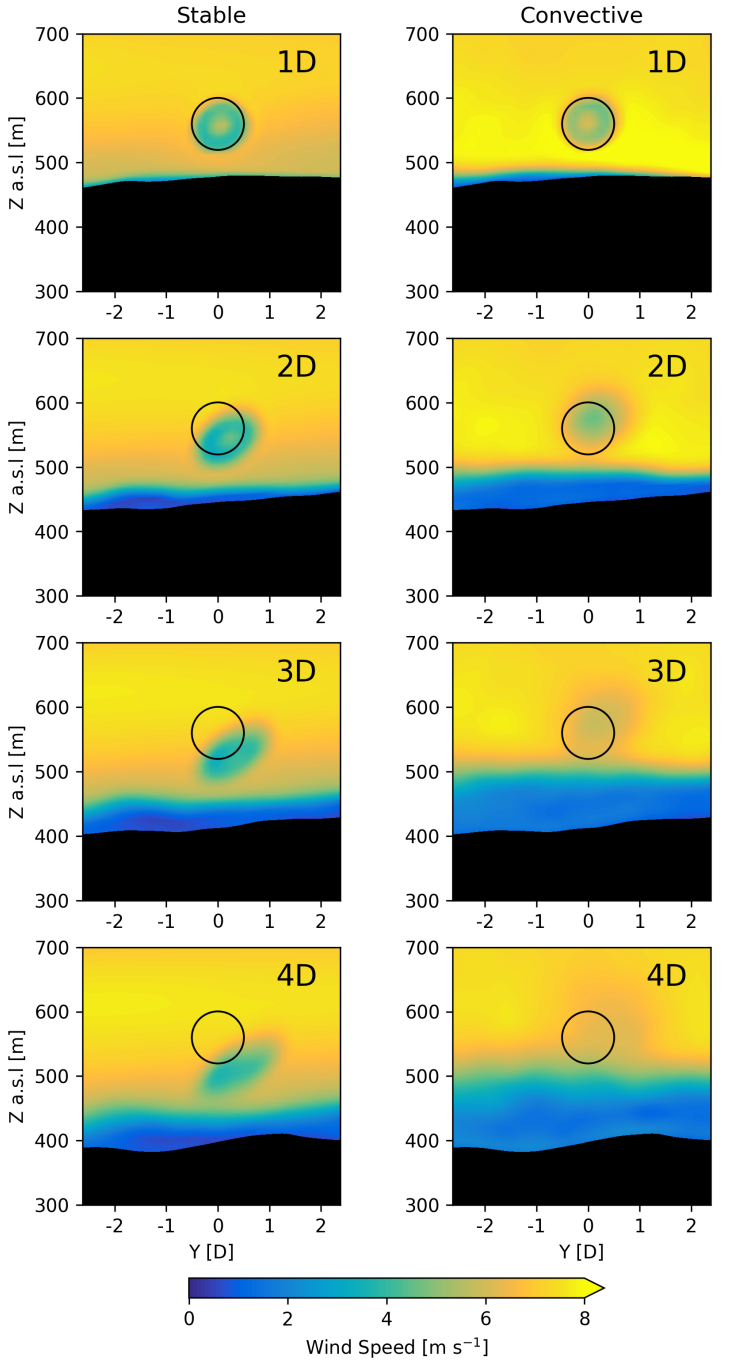

Figure 13. 1 h time-averaged wind speed at different downstream distances for the stable and convective case studies taken along the Wake Transect in Fig. 1. The black circle represents the circumference of the wind turbine rotor at a constant height a.s.l.

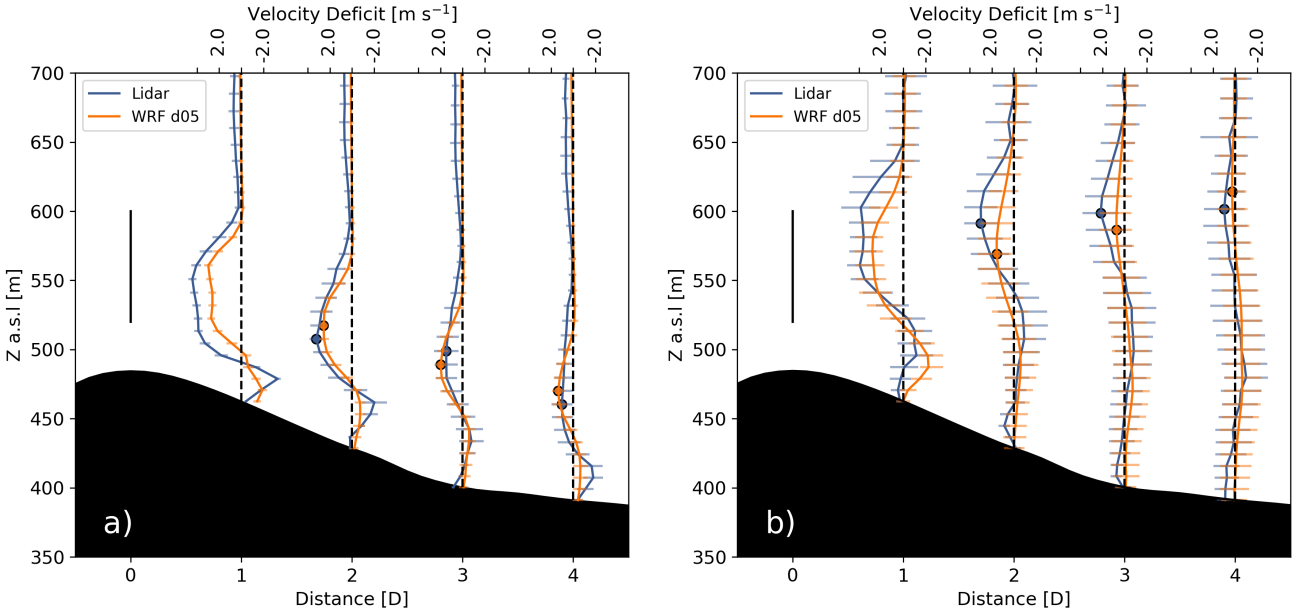

Figure 14. 1 h time-averaged profiles of velocity deficit ~~profiles at different downstream distances~~ along the Wake Transect based on the lidar measurements and calculated in WRF-LES-GAD d05 for the (a) stable and (b) convective case studies. The error bars correspond to $\pm\sigma$, where σ is the standard deviation during the averaging period. The solid black line represents the diameter of the wind turbine rotor.

downwards nearly 100 m in the model and 90 m in the measurements at 4D downstream. ~~An~~ At the same downstream distance, for the convective case, the wake deflects upwards above the hub-height as high as 54 m in the model and 42 m in the measurements. Additionally, an acceleration occurs in the velocity profiles for both case studies below the wake. ~~This behavior was seen in the LES simulations of Vanderwende et al. (2016). This~~ This speedup is more apparent for the stable case, but is still clear for the convective case in the near wake. While the speedup could be due to the small differences in terrain between the two transects, it is more likely due to flow being channeled beneath the wake and above the slower near-surface wind speeds; this is consistent with the observation that this near-surface speedup ~~occurred~~ occurs in LES of wakes in flat terrain (Vanderwende et al., 2016). ~~The differences in the velocity deficit upstream of the wind turbine are due to induction (Medici et al., 2011; Simley et al., 2016) or terrain effects.~~

5 Conclusions

The ~~WRF~~ multi-scale WRF-LES-GAD modeling framework has been used ~~to successfully~~ here to simulate wind turbine wake propagation in complex terrain under different atmospheric stability conditions~~. WRF has been augmented to include a generalized actuator disk (GAD) model to represent individual wind turbine rotors. We used two configurations of WRF-LES-GAD. The first configuration is a single-domain, semi-idealized large-eddy simulation setup in which geostrophic wind speed, wind~~

direction, and potential temperature profiles are specified and atmospheric stability is controlled by specifying a surface heat flux or cooling rate. The second configuration is a multi-scale, nested approach in which WRF-LES-GAD has five domains with grid resolutions of 6750, 2250, 150, 50, and with horizontal grid resolutions ranging from 6750 m on the mesoscale domain to 10 m , with the coarsest two grids being meso-scale simulations and the finest three as micro-scale LES . Note that the first configuration was only used as a preliminary tool to determine whether the more computationally expensive multi-scale setup would likely capture the terrain-induced flow phenomena of interest.

This is, to for the finest LES domain. This setup allows the simulations to capture the interplay between terrain, atmospheric stability, and wind turbine wake dynamics. To the authors' knowledge, this study is the first to combine the first study in which the effects of highly complex terrain are combined with a wind turbine GAD parameterization for real large-eddy simulations in non-neutral stability conditionsto capture the complex interplay between terrain, atmospheric stability, and a wind turbine wake. This novel . The WRF-LES-GAD framework was applied to two case studies: a stable case study where with a mountain wave was present and a convective case study where with a recirculation zoneformed and interacted with the wake. Further, we validated our simulations by comparison , and the simulations were compared to field observations with from both in situ and remote sensing instrumentation.

In the stable case, the wind turbine wake is advected downwarddeflected downward, following the terrain along with the mountain wave. The general characteristics of the mountain wave are were well-captured by the model over the extent of the roughly 8 km domain in comparisons with meteorological towers, a tethered lifting system, radiosonde, and lidar data. The wind speeds within the wave were slightly underestimated, which resulted in under-prediction of the wavelength for the mountain wave. Notably, the mountain wave caused the wake to deflect downwards into the valley. At four rotor diameters downstream of the wind turbine, the wake deflected downwards on average by nearly 100 m below the hub-height, consistent with observations. Further, the stable wake stretches structure stretched from a circular wake into an ellipse due to veer in the stable wind profile. Downwind from the turbine, a near-surface jet is created between the surface and the wake with winds increasing by ~0.25 m s^{-1}.

In the convective case, the wake is was lofted above the terrain and above the original elevation of the wake as a result of the recirculation zone that forms formed in the lee of the first ridge. During this period, the near surface flow can be characterized by a negative potential temperature gradient indicating convective or unstable conditions. The TLS was not operational during this period; therefore, the model was strictly validated against the meteorological towers and a single sounding, followed by comparisons with lidar scans. With unstable thermal stratification, a mountain wake formed in the lee of the first ridge. Averaged over the hour, we observed a 500 m long recirculation zone in the valley, consistent with observations. The formation of a recirculation zone resulted in the wind turbine wake deflecting upwards. The lack of mixing between the wake and recirculation zone resulted in the wake deflecting wake deflected an average of 54 m above hub-height at four rotor diameters downstream. , compared to 42 m in the lidar data. In the convective case, the wake maintains a circular structure downwind but diffuses more rapidly than in the stable case due to increased ambient turbulence. Small speedups of ~0.1 m s^{-1} also occur under the wake as it propagates downwind.

The WRF-LES-GAD framework presented here exhibits ~~remarkably~~ good agreement with field observations during the Perdigão field campaign, ~~making it well-suited to examine the role of complex flow phenomena on wind turbine and wind farm dynamics~~demonstrating its suitability for examining turbine-airflow interactions and wake evolution in realistic settings involving complex terrain and varying atmospheric stability. The ability of the model to capture different wind turbine wake behavior over complex terrain under stable and convective conditions indicates the model's ability to integrate both mesoscale~~and~~ , i.e., regional winds and stability, and local micro-scale flow phenomena which influence the wake behavior. We expect that the conclusions in terms of the wind turbine wake behavior would hold for most convective and stable atmospheric conditions at the Perdigão site as long as the phenomena of interest (recirculation zones and mountain waves) are present. ~~Other~~ Other flow phenomena could be modeled using the multi-scale WRF-LES-GAD framework to examine wind turbine wake behavior ~~in other cases. With regards to other sites, the wind turbine wake behavior would depend largely on the vegetation (surface roughness) and steepness of the terrain.~~ under other conditions.

~~Further studies of interest~~ Further studies at the Perdigão site may also include comparisons with observed turbulence quantities. Of particular interest is the effect of turbulence closure models (Kirkil et al., 2012; Zhou and Chow, 2012) on the detailed behavior of the ~~wind turbine wake and background turbulence . Additionally, it is important to examine the role of turbulence closure models on wake dissipation and recovery. The present study demonstrates the viability of WRF-LES-GAD to model not only flow in complex terrain, but also the flow's interaction with~~ background turbulence and its interactions with the wind turbine wake. As more wind ~~turbine wakes. As more~~ turbines are sited in complex terrain, WRF-LES-GAD will be a useful tool for modeling ~~wake dynamics in such environments, and under different atmospheric forcing regimes~~the effects of surface roughness, terrain steepness, and atmospheric forcing on wake dynamics in these environments.

Data availability. The full WRF-LES-GAD simulation data is several terabytes but subsets of the data can be shared upon request. The input files are available online at https://doi.org/10.5281/zenodo.4711606

Video supplement. The following is available online at https://doi.org/10.5281/zenodo.4711606, Video 1: Multi-scale simulation of a wind turbine wake modulated by a mountain wave in stable atmospheric conditions, along-transect velocity for the entire domain. Video 2: Multi-scale simulation of a wind turbine wake modulated by a mountain wave in stable atmospheric conditions, wind speed and zoomed into the valley. Video 3: Multi-scale simulation of a wind turbine wake modulated by a recirculation zone in convective atmospheric conditions, along-transect velocity for the entire domain.

Appendix A: Sensitivity of Model Results to Grid Resolution

Nested WRF-LES-GAD simulations provide increasingly detailed flow predictions according to the resolution of both the terrain and land-use data, and the ability to resolve turbulent flow structures. Further, nesting from 6750 m to 10 m resolution allows the finest 10 m grid to represent the turbine using the generalized actuator disk model and still be influenced by mesoscale forcing from the larger domains. This appendix quantifies some of the differences between results on different grid nesting levels.

The power spectral density of the 80 m wind speed signals shown in Fig. A1(a) illustrate that higher-frequency turbulence is captured as the grid resolution increases. The spectra are computed using Welch's method (Welch, 1967). The spectra from the measurements at SW_TSE04 roughly follow an inertial subrange slope of -5/3 following Kolmogorov (1941). The spectra for d05 also have an inertial subrange slope of -5/3 and similar energy content to the measurements. Domains d04 and d03 contain a drop-off in the wind speed spectra as is typical of models with finite-difference discretization schemes. The effective resolution for WRF is $\approx 7\Delta x$ (Skamarock, 2004). For wind speeds in the range of 6-8 m s^{-1}, the grid cut-off frequency at the effective resolution is 0.1 Hz, 0.02 Hz, and 0.007 Hz for d05, d04, and d03, respectively. Therefore, only d05 can resolve small-scale features like those observed at SW_TSE04 and that affect wind turbine wake dissipation.

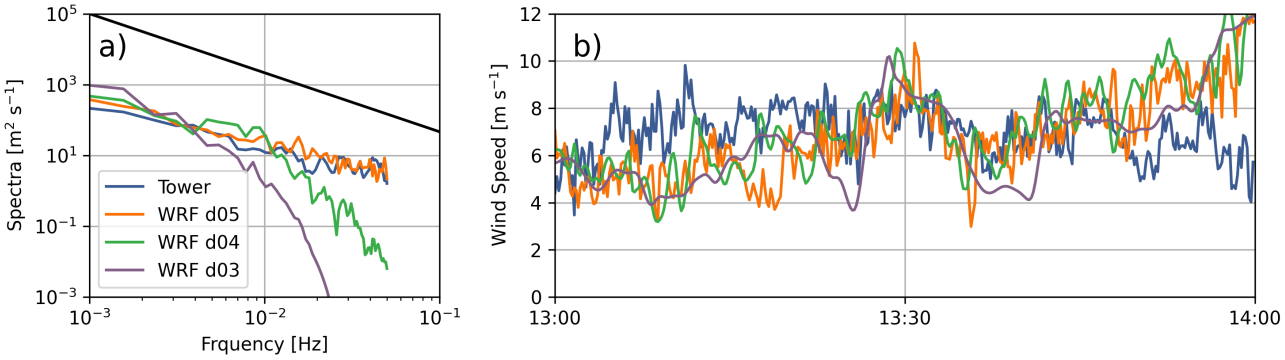

Figure A1. Comparison of (a) time-series and (b) spectra between SW_TSE04 tower data and WRF-LES-GAD d05 ($\Delta x = 10$ m), d04 ($\Delta x = 50$ m) and d03 ($\Delta x = 150$ m) for 80 m wind speed at SW_TSE04 for the convective case study. The -5/3 inertial subrange power law is provided in black for reference. Note that the model wind speed is output at 10 s intervals; therefore, the highest resolvable frequency with this time-series is 0.05 Hz.

Figure A1(b) shows the 80 m wind speed for d05 ($\Delta x = 10$ m), d04 ($\Delta x = 50$ m), and d03 ($\Delta x = 150$ m) as well as the measurements at SW_TSE04 with error metrics in Table A1. The bias and RMSE values for all three domains are similar indicating that there is no significant reduction in errors at this particular location when nesting to finer grid resolution. The errors are driven more by the background flow, which will not change very much between the domains.

In addition to the smaller-scale turbulence resolved on d05, steeper terrain slopes are also resolved on d05 compared to domains d04 and d03. This directly affects whether the flow recirculates in the lee of the first ridge as illustrated in Fig. A2,

Table A1. 80 m wind speed bias and RMSE between WRF-LES-GAD on domains d03, d04, and d05 and SW_TSE04 tower measurements for the convective case study from 13:00 - 14:00 UTC.

80 m Wind Speed (m s^{-1})	
Domain	Bias
RMSE	
WRF d05 (Δx =10 m)	-0.20
2.17	
WRF d04 (Δx =50 m)	0.20
2.28	
WRF d03 (Δx =150 m)	-0.33
2.20	

which shows 1 h time-averaged transects of wind speeds across the wind turbine rotor plane (note that the turbine is only parameterized on d05). While the recirculation zone is resolved on d05 (Fig. A2(a)), the gentler resolved slopes d04 and d03 do not induce recirculation on those domains (Fig. A2(b and c)). Recall that lidar observations in Fig. 9 showed recirculation in the lee of the first ridge. Put together, the effects of increased grid resolution and terrain resolution on d05 provide more accurate representation of the observed flow features including the turbine wake.

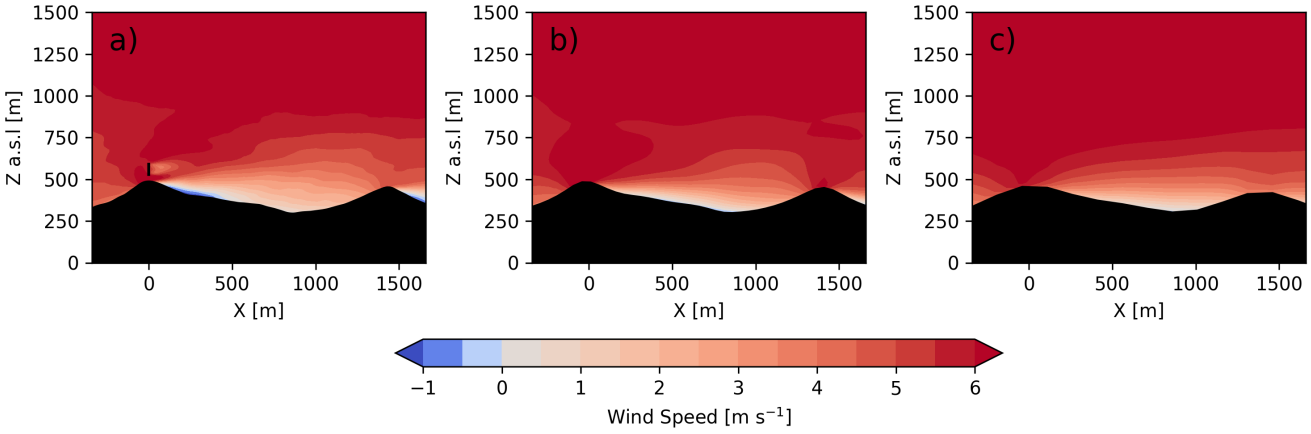

Figure A2. Transect of 1 h time-averaged wind speed for (a) d05 ($\Delta x = 10$ m), (b) d04 ($\Delta x = 50$ m) and (c) d03 ($\Delta x = 150$ m) during the convective case study.

Figure A3 shows wind speed and energy spectra for the stable case study. It is clear in Figure A3(b) that d03 and d04 show wind speeds much smoother than those observed by the tower. The finest domain, d05, is able to capture some fine-scale

turbulent variability in the first and last parts of the 2-hr time period, but not in between. We see this in the spectra in Figure A3(a), where high-frequency turbulence is underestimated in the model compared to the meteorological tower. The energy is shifted to lower-frequencies, thus overestimating the energy content at larger-scales compared to the observations. Note that overall the energy content is lower for the stable compared to the convective case. This, in part, explains why the effect of the grid cut-off frequency is less pronounced compared to Fig A1. Despite the expected limitations of the model to fully capture turbulence in the stable case, we note that the wind turbine wake behavior is largely determined by the mountain wave, which is governed by the internal Froude number and shows limited sensitivity to small-scale turbulence and increasing grid resolution (Figure A4). The bias and RMSE values in Table A2 for all three domains are similar, but do indicate slightly higher bias and RMSE on d05 due to the greater turbulent variability (whereas d03 and d04 are closer to the observed mean velocities but cannot capture the turbulence at all). In conclusion, for the stable case study, large-scale dynamics (the mountain wave) do not require a 10 m grid, but wake and turbulence dynamics do.

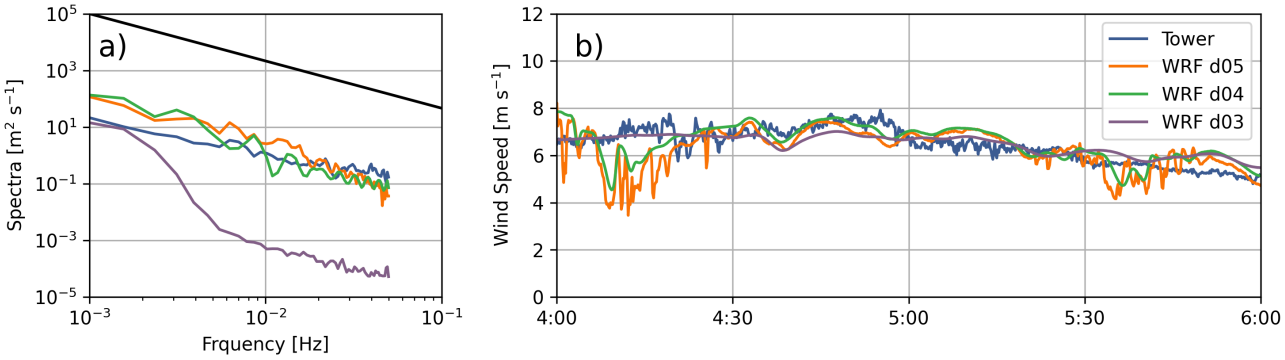

Figure A3. Comparison of (a) time-series and (b) spectra between SW_TSE04 tower data and WRF-LES-GAD d05 ($\Delta x = 10$ m), d04 ($\Delta x = 50$ m) and d03 ($\Delta x = 150$ m) for 80 m wind speed at SW_TSE04 for the stable case study. The -5/3 inertial subrange power law is provided in black for reference. Note that the model wind speed is output at 10 s intervals; therefore, the highest resolvable frequency with this time-series is 0.05 Hz.

Author contributions. Writing—original draft preparation and visualization, ASW; writing—review and editing, JMTN, RSA, JDM, JKL, and FKC; methodology, software, validation, and formal analysis, ASW, JMTN, RSA, and JDM; conceptualization, ASW, JMTN, and FKC; investigation and data curation, JKL. All authors contributed with critical feedback on this research and have read and agreed to the published version of the manuscript.

Competing interests. The authors declare that they have no conflict of interest.

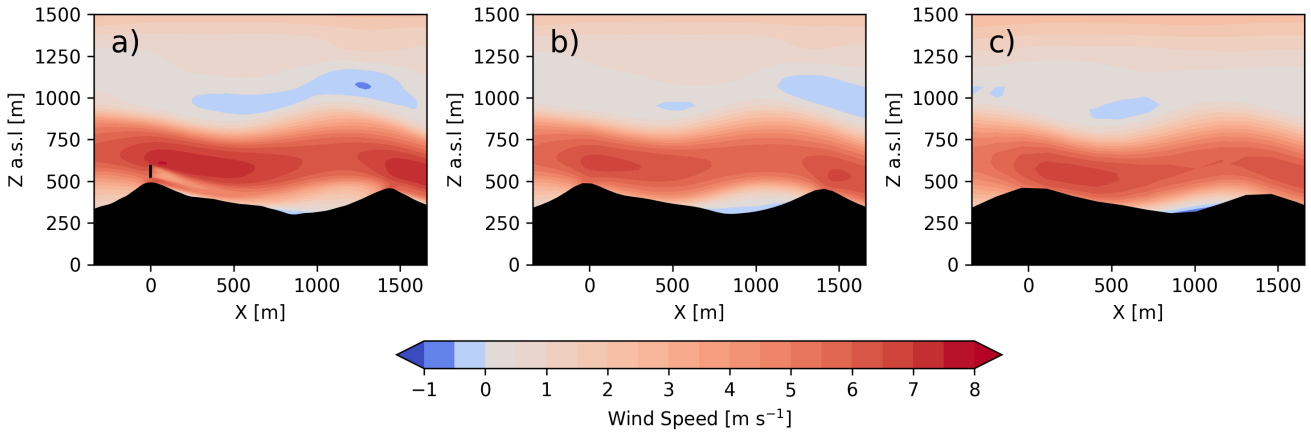

Figure A4. Transect of 1 h time-averaged wind speed for (a) d05 ($\Delta x = 10$ m), (b) d04 ($\Delta x = 50$ m) and (c) d03 ($\Delta x = 150$ m) during the stable case study.

Table A2. 80 m wind speed bias and RMSE between WRF-LES-GAD on domains d03, d04, and d05 and SW_TSE04 tower measurements for the stable case study from 4:00 - 6:00 UTC.

80 m Wind Speed (m s^{-1})	
Domain	Bias
RMSE	
WRF d05 (Δx =10 m)	-0.22
0.83	
WRF d04 (Δx =50 m)	0.07
0.63	
WRF d03 (Δx =150 m)	0.04
0.46	

Acknowledgements. Correspondence with Norman Wildmann from DLR and Robert Menke of DTU regarding their lidar datasets was greatly appreciated. This material is based upon work by ASW supported by the National Science Foundation Graduate Research Fellowship Program under Grant No. DGE 1752814. The authors are grateful for support from National Science Foundation Grants AGS-1565483 and AGS-1565498. The Perdigão was primarily funded by the U.S. National Science Foundation, European Commission's ERANET+, Danish Energy Agency, German Federal Ministry of Economy and Energy, Portugal Foundation for Science and Technology, U.S. Army Research Laboratory, and the Israel Binational Science Foundation. Perdigão would not have been possible without the alliance of many personnel and entities, which are listed in the supplemental material of Fernando et al. (2019). The TLS data presented here were collected by Ludovic Bariteau, Dr. Jessica Tomaszewski, Dr. Nicola Bodini, and Patrick Murphy. RSA's and JDM's contributions were prepared by Lawrence Livermore National Laboratory under Contract DE-AC52-07NA27344, with support from the U.S. DOE Office of Energy Efficiency and

Renewable Energy Wind Energy Technologies Office. This work was authored [in part] by the National Renewable Energy Laboratory, operated by Alliance for Sustainable Energy, LLC, for the U.S. Department of Energy (DOE) under Contract No. DE-AC36-08GO28308. Funding provided by the U.S. Department of Energy Office of Energy Efficiency and Renewable Energy Wind Energy Technologies Office. The views expressed in the article do not necessarily represent the views of the DOE or the U.S. Government. The U.S. Government retains and the publisher, by accepting the article for publication, acknowledges that the U.S. Government retains a nonexclusive, paid-up, irrevocable, worldwide license to publish or reproduce the published form of this work, or allow others to do so, for U.S. Government purposes. High-performance computing support from Cheyenne (doi:10.5065/D6RX99HX) was provided by NCAR's Computational and Information Systems Laboratory, sponsored by the National Science Foundation.

References

Abkar, M. and Porté-Agel, F.: The effect of atmospheric stability on wind-turbine wakes: A large-eddy simulation study, Journal of Physics: Conference Series, 524, 012 138, https://doi.org/10.1088/1742-6596/524/1/012138, 2014.

Abkar, M., Sharifi, A., and Porté-Agel, F.: Wake flow in a wind farm during a diurnal cycle, Journal of Turbulence, 17, 420–441, https://doi.org/10.1080/14685248.2015.1127379, 2016.

Aitken, M. L., Kosović, B., Mirocha, J. D., and Lundquist, J. K.: Large eddy simulation of wind turbine wake dynamics in the stable boundary layer using the Weather Research and Forecasting Model, Journal of Renewable and Sustainable Energy, 6, 033 137, https://doi.org/10.1063/1.4885111, 2014.

Arthur, R. S., Mirocha, J. D., Marjanovic, N., Hirth, B. D., Schroeder, J. L., Wharton, S., and Chow, F. K.: Multi-Scale Simulation of Wind Farm Performance during a Frontal Passage, Atmosphere, 11, 245, https://doi.org/10.3390/atmos11030245, 2020.

Baines, P. G.: Topographic effects in stratified flows: Chapter 6 Stratified flow past three-dimensional topography, pp. 344–443, Cambridge University Press, 1998.

Balsley, B. B.: The CIRES Tethered Lifting System: a survey of the system, past results and future capabilities, Acta Geophysica, 56, 21–57, https://doi.org/10.2478/s11600-007-0045-z, 2008.

Barthelmie, R. J. and Pryor, S. C.: Automated wind turbine wake characterization in complex terrain, Atmospheric Measurement Techniques, 12, 3463–3484, https://doi.org/10.5194/amt-12-3463-2019, 2019.

Berg, J., Troldborg, N., Sørensen, N., Patton, E. G., and Sullivan, P. P.: Large-Eddy Simulation of turbine wake in complex terrain, Journal of Physics: Conference Series, 854, 012 003, https://doi.org/10.1088/1742-6596/854/1/012003, 2017.

Bhaganagar, K. and Debnath, M.: Implications of Stably Stratified Atmospheric Boundary Layer Turbulence on the Near-Wake Structure of Wind Turbines, Energies, 7, 5740–5763, https://doi.org/10.3390/en7095740, 2014.

Bhaganagar, K. and Debnath, M.: The effects of mean atmospheric forcings of the stable atmospheric boundary layer on wind turbine wake, Journal of Renewable and Sustainable Energy, 7, 013 124, https://doi.org/10.1063/1.4907687, 2015.

Bodini, N., Zardi, D., and Lundquist, J. K.: Three-dimensional structure of wind turbine wakes as measured by scanning lidar, Atmospheric Measurement Techniques, 10, 2881–2896, https://doi.org/10.5194/amt-10-2881-2017, 2017.

Bodini, N., Lundquist, J. K., and Optis, M.: Can machine learning improve the model representation of turbulent kinetic energy dissipation rate in the boundary layer for complex terrain?, Geoscientific Model Development, 13, 4271–4285, https://doi.org/10.5194/gmd-13-4271-2020, 2020.

Bossard, M., Feranec, J., Otahel, J., et al.: CORINE land cover technical guide: Addendum 2000, Tech. rep., 2000.

Bromm, M., Vollmer, L., and Kühn, M.: Numerical investigation of wind turbine wake development in directionally sheared inflow, Wind Energy, 20, 381–395, https://doi.org/https://doi.org/10.1002/we.2010, 2017.

Chen, F. and Dudhia, J.: Coupling an advanced land surface-hydrology model with the Penn State-NCAR MM5 modeling system. Part I: Model implementation and sensitivity, Monthly Weather Review, 129, 569–585, 2001.

Chow, F., Schär, C., Ban, N., Lundquist, K., Schlemmer, L., and Shi, X.: Crossing Multiple Gray Zones in the Transition from Mesoscale to Microscale Simulation over Complex Terrain, Atmosphere, 10, 274, https://doi.org/10.3390/atmos10050274, 2019.

Churchfield, M. J. and Sirnivas, S.: On the Effects of Wind Turbine Wake Skew Caused by Wind Veer, https://doi.org/10.2514/6.2018-0755, 2018.

Clyne, J., Mininni, P., Norton, A., and Rast, M.: Interactive desktop analysis of high resolution simulations: application to turbulent plume dynamics and current sheet formation, New Journal of Physics, 9, 301, 2007.

Connolly, A., van Veen, L., Neher, J., Geurts, B. J., Mirocha, J., and Chow, F. K.: Efficacy of the Cell Perturbation Method in Large-Eddy Simulations of Boundary Layer Flow over Complex Terrain, Atmosphere, 12, https://doi.org/10.3390/atmos12010055, 2021.

Dahlberg, J., Poppen, M., and Thor, S.: Load/fatigue effects on a wind turbine generator in a wind farm, Journal of Wind Engineering and Industrial Aerodynamics, 39, 199 – 209, https://doi.org/https://doi.org/10.1016/0167-6105(92)90546-M, 1992.

Daniels, M. H., Lundquist, K. A., Mirocha, J. D., Wiersema, D. J., and Chow, F. K.: A New Vertical Grid Nesting Capability in the Weather Research and Forecasting (WRF) Model, Monthly Weather Review, 144, 3725–3747, https://doi.org/10.1175/MWR-D-16-0049.1, 2016.

Dar, A. S., Berg, J., Troldborg, N., and Patton, E. G.: On the self-similarity of wind turbine wakes in a complex terrain using large eddy simulation, Wind Energy Science, 4, 633–644, https://doi.org/10.5194/wes-4-633-2019, 2019.

Deardorff, J. W.: Stratocumulus-capped mixed layers derived from a three-dimensional model, Boundary-Layer Meteorology, 18, 495–527, 1980.

Draxl, C., Worsnop, R. P., Xia, G., Pichugina, Y., Chand, D., Lundquist, J. K., Sharp, J., Wedam, G., Wilczak, J. M., and Berg, L. K.: Mountain waves can impact wind power generation, Wind Energy Science, 6, 45–60, https://doi.org/10.5194/wes-6-45-2021, 2021.

Dudhia, J.: Numerical study of convection observed during the winter monsoon experiment using a mesoscale two-dimensional model, Journal of the Atmospheric Sciences, 46, 3077–3107, 1989.

Dörenkämper, M., Witha, B., Steinfeld, G., Heinemann, D., and Kühn, M.: The impact of stable atmospheric boundary layers on wind-turbine wakes within offshore wind farms, Journal of Wind Engineering and Industrial Aerodynamics, 144, 146–153, https://doi.org/10.1016/j.jweia.2014.12.011, 2015.

Englberger, A. and Dörnbrack, A.: Wind-turbine wakes responding to stably stratified flow over complex terrain, Journal of Physics: Conference Series, 1037, 072 014, https://doi.org/10.1088/1742-6596/1037/7/072014, 2018.

Englberger, A. and Lundquist, J. K.: How does inflow veer affect the veer of a wind-turbine wake?, Journal of Physics, 1452, 012 068, https://doi.org/doi:10.1088/1742-6596/1452/1/012068, 2020.

Farr, T. G., Rosen, P. A., Caro, E., Crippen, R., Duren, R., Hensley, S., Kobrick, M., Paller, M., Rodriguez, E., Roth, L., et al.: The shuttle radar topography mission, Reviews of Geophysics, 45, 2007.

Fernando, H. J. S., Mann, J., Palma, J. M. L. M., Lundquist, J. K., Barthelmie, R. J., Belo-Pereira, M., Brown, W. O. J., Chow, F. K., Gerz, T., Hocut, C. M., Klein, P. M., Leo, L. S., Matos, J. C., Oncley, S. P., Pryor, S. C., Bariteau, L., Bell, T. M., Bodini, N., Carney, M. B., Courtney, M. S., Creegan, E. D., Dimitrova, R., Gomes, S., Hagen, M., Hyde, J. O., Kigle, S., Krishnamurthy, R., Lopes, J. C., Mazzaro, L., Neher, J. M. T., Menke, R., Murphy, P., Oswald, L., Otarola-Bustos, S., Pattantyus, A. K., Rodrigues, C. V., Schady, A., Sirin, N., Spuler, S., Svensson, E., Tomaszewski, J., Turner, D. D., van Veen, L., Vasiljević, N., Vassallo, D., Voss, S., Wildmann, N., and Wang, Y.: The Perdigão: Peering into Microscale Details of Mountain Winds, Bulletin of the American Meteorological Society, 100, 799–819, https://doi.org/10.1175/BAMS-D-17-0227.1, 2019.

Fitch, A. C., Olson, J. B., and Lundquist, J. K.: Parameterization of Wind Farms in Climate Models, Journal of Climate, 26, 6439 – 6458, https://doi.org/10.1175/JCLI-D-12-00376.1, 2013.

Frandsen, S. and Christensen, C.: Structural loads in large wind farm arrays, European Wind Energy Conference and Exhibition, EWEC '94, conference date: 09-10-1994 Through 13-10-1994, 1994.

Frandsen, S. and Thomsen, K.: Change in Fatigue and Extreme Loading when Moving Wind Farms Offshore, Wind Engineering, 21, 197–214, http://www.jstor.org/stable/43749643, 1997.

Haupt, S. E., Kosović, B., Shaw, W., Berg, L. K., Churchfield, M., Cline, J., Draxl, C., Ennis, B., Koo, E., Kotamarthi, R., Mazzaro, L., Mirocha, J., Moriarty, P., Muñoz-Esparza, D., Quon, E., Rai, R. K., Robinson, M., and Sever, G.: On Bridging A Modeling Scale Gap: Mesoscale to Microscale Coupling for Wind Energy, Bulletin of the American Meteorological Society, 100, 2533–2550, https://doi.org/10.1175/BAMS-D-18-0033.1, 2019.

Hirth, B. and Schroeder, J.: Documenting Wind Speed and Power Deficits behind a Utility-Scale Wind Turbine, Journal of Applied Meteorology and Climatology, 52, 39–46, https://doi.org/10.1175/JAMC-D-12-0145.1, 2013.

Iungo, G. V., Wu, Y.-T., and Porté-Agel, F.: Field Measurements of Wind Turbine Wakes with Lidars, Journal of Atmospheric and Oceanic Technology, 30, 274–287, https://doi.org/10.1175/JTECH-D-12-00051.1, 2013.

Jackson, P. L., Mayr, G., and Vosper, S.: Mountain weather research and forecasting - recent progress and current challenges: Chapter 3 Dynamically-Driven Winds, pp. 121–218, Springer, New York, 2013.

Kirkil, G., Mirocha, J., Bou-Zeid, E., Chow, F. K., and Kosović, B.: Implementation and Evaluation of Dynamic Subfilter-Scale Stress Models for Large-Eddy Simulation Using WRF*, Monthly Weather Review, 140, 266–284, https://doi.org/10.1175/MWR-D-11-00037.1, 2012.

Kolmogorov, A. N.: The Local Structure of Turbulence in Incompressible Viscous Fluid for Very Large Reynolds' Numbers, in: Dokl. Akad. Nauk SSSR, vol. 30, pp. 301–305, 1941.

Lissaman, P. B. S.: Energy Effectiveness of Arbitrary Arrays of Wind Turbines, Journal of Energy, 3, 323–328, https://doi.org/10.2514/3.62441, 1979.

Lundquist, J. K. and Bariteau, L.: Dissipation of Turbulence in the Wake of a Wind Turbine, Boundary-Layer Meteorology, 154, 229–241, https://doi.org/10.1007/s10546-014-9978-3, 2015.

Lundquist, J. K., Churchfield, M. J., Lee, S., and Clifton, A.: Quantifying error of lidar and sodar Doppler beam swinging measurements of wind turbine wakes using computational fluid dynamics, Atmos. Meas. Tech., 8, 907–920, https://doi.org/10.5194/amt-8-907-2015, 2015.

Marjanovic, N., Mirocha, J. D., Kosović, B., Lundquist, J. K., and Chow, F. K.: Implementation of a generalized actuator line model for wind turbine parameterization in the Weather Research and Forecasting model, Journal of Renewable and Sustainable Energy, 9, 063 308, https://doi.org/10.1063/1.4989443, 2017.

Medici, D., Ivanell, S., Dahlberg, J.-A., and Alfredsson, P. H.: The upstream flow of a wind turbine: blockage effect, Wind Energy, 14, 691–697, https://doi.org/https://doi.org/10.1002/we.451, 2011.

Menke, R., Vasiljević, N., Hansen, K. S., Hahmann, A. N., and Mann, J.: Does the wind turbine wake follow the topography? A multi-lidar study in complex terrain, Wind Energy Science, 3, 681–691, https://doi.org/10.5194/wes-3-681-2018, 2018.

Menke, R., Vasiljević, N., Mann, J., and Lundquist, J. K.: Characterization of flow recirculation zones at the Perdigão site using multi-lidar measurements, Atmospheric Chemistry and Physics, 19, 2713–2723, https://doi.org/10.5194/acp-19-2713-2019, 2019.

Menke, R., Vasiljević, N., Wagner, J., Oncley, S. P., and Mann, J.: Multi-lidar wind resource mapping in complex terrain, Wind Energy Science, 5, 1059–1073, https://doi.org/10.5194/wes-5-1059-2020, 2020.

Mirocha, J. D., Kosović, B., Aitken, M. L., and Lundquist, J. K.: Implementation of a generalized actuator disk wind turbine model into the weather research and forecasting model for large-eddy simulation applications, Journal of Renewable and Sustainable Energy, 6, 013 104, https://doi.org/10.1063/1.4861061, 2014.

Mirocha, J. D., Rajewski, D. A., Marjanovic, N., Lundquist, J. K., Kosović, B., Draxl, C., and Churchfield, M. J.: Investigating wind turbine impacts on near-wake flow using profiling lidar data and large-eddy simulations with an actuator disk model, Journal of Renewable and Sustainable Energy, 7, 043 143, https://doi.org/10.1063/1.4928873, 2015.

Mlawer, E. J., Taubman, S. J., Brown, P. D., Iacono, M. J., and Clough, S. A.: Radiative transfer for inhomogeneous atmospheres: RRTM, a validated correlated-k model for the longwave, Journal of Geophysical Research: Atmospheres, 102, 16 663–16 682, 1997.

Muñoz-Esparza, D., Kosović, B., Mirocha, J., and van Beeck, J.: Bridging the transition from mesoscale to microscale turbulence in numerical weather prediction models, Boundary-Layer Meteorology, 153, 409–440, 2014.

Muñoz-Esparza, D., Kosović, B., Van Beeck, J., and Mirocha, J.: A stochastic perturbation method to generate inflow turbulence in large-eddy simulation models: Application to neutrally stratified atmospheric boundary layers, Physics of Fluids, 27, 035 102, 2015.

Muñoz-Esparza, D. and Kosović, B.: Generation of Inflow Turbulence in Large-Eddy Simulations of Nonneutral Atmospheric Boundary Layers with the Cell Perturbation Method, Monthly Weather Review, 146, 1889–1909, https://doi.org/10.1175/MWR-D-18-0077.1, 2018.

Muñoz-Esparza, D., Lundquist, J. K., Sauer, J. A., Kosović, B., and Linn, R. R.: Coupled mesoscale-LES modeling of a diurnal cycle during the CWEX-13 field campaign: From weather to boundary-layer eddies, Journal of Advances in Modeling Earth Systems, 9, 1572–1594, https://doi.org/https://doi.org/10.1002/2017MS000960, 2017.

Nakanishi, M. and Niino, H.: An improved Mellor–Yamada level-3 model: Its numerical stability and application to a regional prediction of advection fog, Boundary-Layer Meteorology, 119, 397–407, 2006.

Nakanishi, M. and Niino, H.: Development of an Improved Turbulence Closure Model for the Atmospheric Boundary Layer, Journal of the Meteorological Society of Japan. Ser. II, 87, 895–912, https://doi.org/10.2151/jmsj.87.895, 2009.

National Centers for Environmental Prediction, National Weather Service, NOAA, U.S. Department of Commerce: NCEP GFS 0.25 Degree Global Forecast Grids Historical Archive, https://doi.org/10.5065/D65D8PWK, 2015.

Palma, J. M. L. M., Silva, C. A. M., Gomes, V. M. C., Silva Lopes, A., Simões, T., Costa, P., and Batista, V. T. P.: The digital terrain model in the computational modelling of the flow over the Perdigão site: the appropriate grid size, preprint, Wind and turbulence, https://doi.org/10.5194/wes-2019-96, 2020.

Pineda, N., Jorba, O., Jorge, J., and Baldasano, J.: Using NOAA AVHRR and SPOT VGT data to estimate surface parameters: application to a mesoscale meteorological model, International Journal of Remote Sensing, 25, 129–143, 2004.

Porté-Agel, F., Bastankhah, M., and Shamsoddin, S.: Wind-Turbine and Wind-Farm Flows: A Review, Boundary-Layer Meteorology, 174, 1–59, https://doi.org/10.1007/s10546-019-00473-0, 2020.

Powers, J. G., Klemp, J. B., Skamarock, W. C., Davis, C. A., Dudhia, J., Gill, D. O., Coen, J. L., Gochis, D. J., Ahmadov, R., Peckham, S. E., Grell, G. A., Michalakes, J., Trahan, S., Benjamin, S. G., Alexander, C. R., Dimego, G. J., Wang, W., Schwartz, C. S., Romine, G. S., Liu, Z., Snyder, C., Chen, F., Barlage, M. J., Yu, W., and Duda, M. G.: The Weather Research and Forecasting Model: Overview, System Efforts, and Future Directions, Bulletin of the American Meteorological Society, 98, 1717 – 1737, https://doi.org/10.1175/BAMS-D-15-00308.1, 2017.

Rogers, E., Black, T., Ferrier, B., Lin, Y., Parrish, D., and DiMego, G.: National Oceanic and Atmospheric Administration Changes to the NCEP Meso Eta Analysis and Forecast System: Increase in resolution, new cloud microphysics, modified precipitation assimilation, modified 3DVAR analysis., Tech. rep., NOAA), 2001.

Shamsoddin, S. and Porté-Agel, F.: Large-Eddy Simulation of Atmospheric Boundary-Layer Flow Through a Wind Farm Sited on Topography, Boundary-Layer Meteorology, 163, 1–17, https://doi.org/10.1007/s10546-016-0216-z, 2017.

Simley, E., Angelou, N., Mikkelsen, T., Sjöholm, M., Mann, J., and Pao, L. Y.: Characterization of wind velocities in the upstream induction zone of a wind turbine using scanning continuous-wave lidars, Journal of Renewable and Sustainable Energy, 8, 013 301, https://doi.org/10.1063/1.4940025, 2016.

Skamarock, W. C.: Evaluating mesoscale NWP models using kinetic energy spectra, Monthly weather review, 132, 3019–3032, 2004.

Skamarock, W. C., Klemp, J. B., Dudhia, J., Gill, D. O., Barker, D. M., Wang, W., and Powers, J. G.: A description of the advanced research WRF version 3, Tech. rep., NCAR, 2008.

Stevens, R. J. and Meneveau, C.: Flow Structure and Turbulence in Wind Farms, Annual Review of Fluid Mechanics, 49, 311–339, https://doi.org/10.1146/annurev-fluid-010816-060206, 2017.

Stull, R.: An Introduction to Boundary Layer Meteorology: Chapter 14 Geographic Effects, Atmospheric and Oceanographic Sciences Library, Springer Netherlands, https://books.google.com/books?id=eRRz9RNvNOkC, 1988.

Taylor, G. J.: Wake measurements on the Nibe wind turbines in Denmark, Tech. Rep. CEC Contract EN3W.0039.UK(H1), 1990.

Thomsen, K. and Sørensen, P.: Fatigue loads for wind turbines operating in wakes, Journal of Wind Engineering and Industrial Aerodynamics, 80, 121–136, https://doi.org/10.1016/S0167-6105(98)00194-9, 1999.

Tian, W., Ozbay, A., Yuan, W., Sarakar, P., and Hu, H.: An Experimental Study on the Performances of Wind Turbines over Complex Terrains, https://doi.org/10.2514/6.2013-612, 2013.

Vanderwende, B. J., Kosović, B., Lundquist, J. K., and Mirocha, J. D.: Simulating effects of a wind-turbine array using LES and RANS, Journal of Advances in Modeling Earth Systems, 8, 1376–1390, https://doi.org/https://doi.org/10.1002/2016MS000652, 2016.

Veers, P., Dykes, K., Lantz, E., Barth, S., Bottasso, C. L., Carlson, O., Clifton, A., Green, J., Green, P., Holttinen, H., Laird, D., Lehtomäki, V., Lundquist, J. K., Manwell, J., Marquis, M., Meneveau, C., Moriarty, P., Munduate, X., Muskulus, M., Naughton, J., Pao, L., Paquette, J., Peinke, J., Robertson, A., Rodrigo, J. S., Sempreviva, A. M., Smith, J. C., Tuohy, A., and Wiser, R.: Grand challenges in the science of wind energy, Science, 366, eaau2027, https://doi.org/10.1126/science.aau2027, 2019.

Vollmer, L., Lee, J. C.-Y., Steinfeld, G., and Lundquist, J. K.: A wind turbine wake in changing atmospheric conditions: LES and lidar measurements, Journal of Physics: Conference Series, 854, 012 050, https://doi.org/10.1088/1742-6596/854/1/012050, 2017.

Wagner, J., Gerz, T., Wildmann, N., and Gramitzky, K.: Long-term simulation of the boundary layer flow over the double-ridge site during the Perdigão 2017 field campaign, Atmospheric Chemistry and Physics, 19, 1129–1146, https://doi.org/10.5194/acp-19-1129-2019, 2019.

Welch, P.: The use of fast Fourier transform for the estimation of power spectra: a method based on time averaging over short, modified periodograms, IEEE Transactions on audio and electroacoustics, 15, 70–73, https://doi.org/10.1109/TAU.1967.1161901, 1967.

Wendels, W.: Investigation of a nested large eddy simulation of the atmospheric boundary layer over the Perdigão field campaign site, Ph.D. thesis, University of Twente, 2019.

Wiersema, D. J., Lundquist, K. A., and Chow, F. K.: Mesoscale to Microscale Simulations over Complex Terrain with the Immersed Boundary Method in the Weather Research and Forecasting Model, Monthly Weather Review, 148, https://doi.org/10.1175/MWR-D-19-0071.1, 2020.

Wildmann, N., Kigle, S., and Gerz, T.: Coplanar lidar measurement of a single wind energy converter wake in distinct atmospheric stability regimes at the Perdigão 2017 experiment, Journal of Physics: Conference Series, 1037, 052 006, https://doi.org/10.1088/1742-6596/1037/5/052006, 2018.

Wildmann, N., Bodini, N., Lundquist, J. K., Bariteau, L., and Wagner, J.: Estimation of turbulence dissipation rate from Doppler wind lidars and in situ instrumentation for the Perdigão 2017 campaign, Atmospheric Measurement Techniques, 12, 6401–6423, https://doi.org/10.5194/amt-12-6401-2019, 2019.

Wise, A. S., Neher, J. M. T., Arthur, R. S., and Chow, F. K.: Multi-Scale Modeling of a Wind Turbine Wake Over Complex Terrain in Different Atmospheric Stability Regimes, in: 19th Conference of Mountain Meteorology, p. 8.2, https://ams.confex.com/ams/19Mountain/meetingapp.cgi/Session/54552, 2020.

Wyngaard, J. C.: Toward Numerical Modeling in the "Terra Incognita", Journal of the Atmospheric Sciences, 61, 1816–1826, https://doi.org/10.1175/1520-0469(2004)061<1816:TNMITT>2.0.CO;2, 2004.

Xia, G., Draxl, C., Raghavendra, A., and Lundquist, J. K.: Validating simulated mountain wave impacts on hub-height wind speed using SoDAR observations, Renewable Energy, 163, 2220–2230, https://doi.org/https://doi.org/10.1016/j.renene.2020.10.127, 2021.

Zhou, B. and Chow, F. K.: Turbulence Modeling for the Stable Atmospheric Boundary Layer and Implications for Wind Energy, Flow, Turbulence and Combustion, 88, 255–277, https://doi.org/10.1007/s10494-011-9359-7, 2012.